



# Physical properties of the (Tl, Hg)-1223 superconductor phase substituted by lanthanum and samarium fluorides

Rola F. Khattar<sup>1</sup> · K. Habanjar<sup>1</sup> · R. Awad<sup>2</sup> · M. Anas<sup>2</sup>

Received: 20 September 2023 / Accepted: 27 December 2023 / Published online: 26 January 2024  
© The Author(s), under exclusive licence to Springer-Verlag GmbH, DE part of Springer Nature 2024

## Abstract

The effect of samarium and lanthanum fluorides ( $\text{SmF}_3$  and  $\text{LaF}_3$ ) on the structural and superconducting properties of  $\text{Tl}_{0.8}\text{Hg}_{0.2}\text{Ba}_2\text{Ca}_{2-x}\text{R}_x\text{Cu}_3\text{O}_{9-\delta-y}\text{F}_y$  superconducting phase (Tl, Hg)-1223, where  $R = \text{Sm}$  or  $\text{La}$  and  $x = 0.00, 0.025, 0.050, 0.075, \text{ and } 0.10$  was investigated. The solid-state reaction method was used to synthesize the superconducting samples. The phase formation percentages and lattice parameters were calculated using X-ray powder diffraction (XRD). Images taken with a scanning electron microscope (SEM) show that the presence of both Sm and La increases the grain size and inter-grain connectivity up to  $x = 0.025$ . The successful substitution of Sm and La elements in the crystal structure of (Tl, Hg)-1223 is confirmed by energy-dispersive X-ray (EDX) analysis. The oxidation states of the elements in the prepared samples are revealed by X-ray photoelectron spectroscopy (XPS) spectra.  $I$ - $V$  and resistivity measurements were used to investigate the electrical properties of the (Tl, Hg)-1223 system with Sm and La substitutions. The superconducting transition temperature ( $T_c$ ) and transport critical current density ( $J_c$ ) have steadily improved up to  $x = 0.025$ , above which they dropped significantly. Furthermore, as temperature increased, the temperature dependence of fluctuation conductivity ( $\Delta\sigma$ ), revealed distinct zones. The zero-temperature coherence length ( $\xi_c(0)$ ), effective layer thickness of the two-dimensional system ( $d$ ), interlayer coupling ( $I$ ), Fermi velocity ( $v_f$ ), and Fermi energy ( $E_f$ ) were determined.  $\xi_c(0)$  and  $d$  decrease until  $x = 0.025$ , then increase as  $x$  increases. All estimated  $I$  values show weak coupling between  $\text{CuO}_2$  planes and a transition from three-dimensional (3D) to two-dimensional (2D) regions.

**Keywords** (Tl, Hg)-1223 phase · ( $\text{SmF}_3$  and  $\text{LaF}_3$ ) substitution · Superconducting properties · XPS · Excess conductivity

## 1 Introduction

Thallium (Tl) and mercury (Hg)-based superconductors are receiving a lot of attention owing to their remarkable  $T_c$  records of 125 K and 135 K at normal pressure, respectively. [1, 2]. From a scientific standpoint, these superconducting oxides are fascinating, having a lot of potential for use in electrical devices like Josephson junctions and superconducting transistors [3, 4]. This is due to their high  $T_c$  and the ability to operate and be controlled at 77 K, the temperature

of liquid nitrogen. Mercury and thallium, on the other hand, are extremely toxic and unstable at high temperatures [5, 6]. Furthermore, achieving a high-purity superconducting phase is highly dependent on the precursor and synthesis conditions [5].

For the improvement of their physical properties, the partial chemical substitution in high-temperature superconductors (HTSCs) is considered an effective tool for this purpose. The generation of new effective flux pinning centers enhanced  $T_c$  as well as the current density  $J_c$  [7, 8]. Many studies have been conducted to investigate the effect of chemical substitutions at the calcium (Ca)-site on cuprate superconductors. [9–12]. Arif et al. [9] investigated the effect of Ti substitution on  $(\text{Cu}_{0.5}\text{Tl}_{0.5})\text{Ba}_2(\text{Ca}_{2-x}\text{Ti}_x)\text{Cu}_3\text{O}_{10-\delta}$  (for  $x = 0, 0.25, 0.5$  and  $0.75$ ) superconducting samples. The values of  $T_c$  and cross-over temperature ( $T_G$ ) were improved, and the superconducting anisotropy is minimized when Ti atoms with a lower ionic radius than Ca atoms are added between the  $\text{CuO}_2$  planes. Khan

Rola F. Khattar and K. Habanjar have the same contribution.

✉ K. Habanjar  
k.habanjar@bau.edu.lb

<sup>1</sup> Department of Physics, Faculty of Science, Beirut Arab University, Beirut, Lebanon

<sup>2</sup> Department of Physics, Faculty of Science, Alexandria University, Alexandria, Egypt

et al. [10] studied the partial replacement of  $\text{Ca}^{2+}$  ions by magnesium ions ( $\text{Mg}^{2+}$ ) and praseodymium ions ( $\text{Pr}^{3+}$ ) in  $(\text{Cu}_{0.5}\text{Tl}_{0.5})\text{Ba}_2\text{Ca}_{2-y}\text{M}_y\text{Cu}_3\text{O}_{10-\delta}$  ( $\text{M} = \text{Pr}$  and  $\text{Mg}$ ). The results showed that Mg substitution enhanced the inter-plane coupling, decreased the lattice parameter  $c$ , improved  $J_c$  and  $T_c$ , and softened the apical oxygen mode. On the other hand, Pr substitution increased the lattice parameter  $c$ , increased  $\text{CuO}_2$ -plane decoupling, and decreased  $T_c$ . Moreover, according to Erbilin et al. [11], a low vanadium replacement for Ca sites in Tl-2223 superconductor enhanced  $T_c$ . Boudjadja et al. [12] studied how yttrium doping influences the structural and electrical properties of  $\text{Bi}_2\text{Sr}_{1.9}\text{Ca}_{0.1-x}\text{Y}_x\text{Cu}_2\text{O}_{7+\delta}$  (Bi-2202) cuprate ceramics. The results provide valuable insights into alterations in resistivity concerning temperature variations, specifically attributed to calcium (Ca) substitutions.

Rare-earth element substitutions improved superconductivity at low replacement content but degraded it as substitution concentration increased [13, 14]. Several studies have investigated the impact of rare-earth element substitutions on different HTSC phases [15–21]. Bakar et al. [15] investigated the effect of thallium substitutions on the superconducting phase of  $(\text{Tl}_{0.7}\text{M}_{0.3})\text{Sr}_2\text{CaCu}_2\text{O}_7$ , where  $\text{M} = \text{Er}$ ,  $\text{Gd}$ ,  $\text{La}$ ,  $\text{Na}$ ,  $\text{K}$ , and  $\text{Rb}$ . Rare-earth substitutions with smaller ionic radii were found to reduce flux pinning and impair inter-granular coupling more than rare-earth substitutions with larger ionic radii. Awad et al. [16] studied superconducting materials of the type  $\text{TlBa}_2\text{Ca}_{2-x}\text{Sc}_x\text{Cu}_3\text{O}_{9-\delta}$  ( $0.0 \leq x \leq 0.6$ ). They discovered that a low scandium content promoted the formation of the Tl-1223 phase and reduced impurity phases. Sm substitution in  $\text{Tl}_{0.8}\text{Hg}_{0.2}\text{Ba}_2\text{Ca}_{2-x}\text{Sm}_x\text{Cu}_3\text{O}_{9-\delta}$  lowered the phase transition temperature while increasing the inter-grain critical density until  $x = 0.05$  and subsequently it decreased [17]. In the (Bi, Pb)-2212 phase, samarium (Sm) substitution enhanced both  $J_c$  and  $T_c$  [18]. Furthermore, the normal-state Hall effect for  $\text{Tl}_{0.8}\text{Hg}_{0.2}\text{Ba}_2\text{Ca}_{2-x}\text{R}_x\text{Cu}_3\text{O}_{9-\delta-y}\text{F}_y$ , where  $\text{R} = \text{Sm}$  and ytterbium (Yb) with  $0 \leq x \leq 0.15$ , was studied by Awad et al. [19]. It was found that the Hall coefficients  $R_H$  are positive and followed the Curie–Weiss temperature dependence type. Lower substitution content Pr and La replacements at Ca sites of  $(\text{Cu}_{0.5}\text{Tl}_{0.5})$ -1223 superconductor phase improved the volume fraction and enhanced the  $T_c$  [20].

Sedky et al. [21] conducted research on the impact of La-substituted Ca on (Bi, Pb):2212 and (Bi, Pb):2223 superconductors, providing valuable insights into the role of La substitution in improving superconductivity. Their findings suggest that La substitution in the 2212 series is particularly well suited for applications requiring increased hardness, critical fields, and currents. Conversely, the 2223 series appears more suitable for research purposes, offering higher transition temperatures ( $T_c$ ) and the potential to alter plastic deformation.

Many researchers studied the effect of fluorine (F) doping on the properties of HTSCs [22–26]. Hamdan et al. [22] investigated the impact of fluorine on  $(\text{Tl}_{0.5}\text{Pb}_{0.5})\text{Sr}_{1.6}\text{Ba}_{0.4}\text{Ca}_2\text{Cu}_3\text{O}_y$ . In comparison to the pure sample, the addition of fluorine boosted the development of the Tl-1223 phase, increased the  $T_c$  to 128 K, and increased the critical current density by the rate of 300%. Anas [23] investigated the effect of  $\text{PbF}_2$  doping on the electrical and mechanical characteristics of the (Bi,Pb)-2223 superconducting phase. The results in both electrical and mechanical aspects showed enhancements in  $T_c$ ,  $J_c$ , and Vickers microhardness  $H_v$ , with optimal values at  $x = 0.1$  doping level. AbuHlaiwa et al. [24] investigated the impact of  $\text{PbF}_2$  substitution on the  $(\text{Cu}_{0.5}\text{Tl}_{0.5})$ -1223 phase, where Cu was substituted with Pb atoms and O was replaced with F in the charge reservoir layers.  $T_c$  was increased to its optimal value for  $x = 0.06$   $\text{PbF}_2$ , after which a reversal trend was seen. They proposed that change in  $T_c$  is closely connected to the replacement of Cu by Pb and variation in oxygen concentration owing to F substitutions. The substitution of oxygen with fluorine has demonstrated a notable enhancement in the superconducting properties of  $(\text{Cu}_{0.5-x}\text{Tl}_{0.5-y})$ -1223 phase doped with  $(\text{CuF}_2)_x$  and  $(\text{TlF})_y$  up to  $x = 0.2$  and  $y = 0.1$  [25]. For (Bi,Pb)-2234, the volume fraction and the flux pinning are well enhanced with  $\text{TlF}_3$  doping [26].

The partial replacement of  $\text{Ca}^{2+}$  ions by  $\text{Sm}^{3+}$  and  $\text{La}^{3+}$  ions is investigated in this work using rare-earth fluorides ( $\text{SmF}_3$  and  $\text{LaF}_3$ ). A series of superconducting samples of type  $\text{Tl}_{0.8}\text{Hg}_{0.2}\text{Ba}_2\text{Ca}_{2-x}\text{R}_x\text{Cu}_3\text{O}_{9-\delta-y}\text{F}_y$  (where  $\text{R} = \text{Sm}$  and  $\text{La}$ ) are synthesized in a sealed quartz tube using a solid-state reaction procedure, with  $x = 0.00, 0.025, 0.050, 0.075$ , and  $0.10$ . To examine the physical and electrical properties of prepared samples, X-ray powder diffraction, scanning electron microscopy, electron dispersive X-ray, X-ray photoelectron spectroscopy, electrical resistivity, and  $I$ - $V$  curves are used.

## 2 Experimental techniques

### 2.1 Samples preparation

$\text{Tl}_{0.8}\text{Hg}_{0.2}\text{Ba}_2\text{Ca}_{2-x}\text{R}_x\text{Cu}_3\text{O}_{9-\delta-y}\text{F}_y$  superconducting samples were prepared via solid-state reaction techniques, where  $\text{R} = \text{Sm}$  and  $\text{La}$  and  $x = 0.00, 0.025, 0.050, 0.075$ , and  $0.10$ . Appropriate weights of  $\text{Tl}_2\text{O}_3$ ,  $\text{HgO}$ ,  $\text{BaO}_2$ ,  $\text{CaO}$ ,  $\text{CuO}$ ,  $\text{SmF}_3$ , and  $\text{LaF}_3$  (Sigma-Aldrich with purity greater than 99%) were measured using a sensitive balance and in proportion to their molecular weights. Additional amounts of 10%  $\text{Tl}_2\text{O}_3$  and  $\text{HgO}$  were introduced to account for the losses of thallium and mercury experienced during the heating process [27].

To achieve a consistently fine mixture, the powders were mixed and ground by using an agate mortar for approximately 30 min. Subsequently, the fine powder was carefully sifted through a 60  $\mu\text{m}$  sieve, ensuring a uniformly fine mixture. The mixture was pelletized using a hydraulic press at a pressure of 10 tons/cm<sup>2</sup> and carefully covered in silver foil to reduce thallium and mercury from evaporating throughout the heating process. The samples were carefully heated in a quartz tube within a box furnace. The heating process followed precise rates: 4 K/min until reaching 993 K, then 2 K/min until hitting 1133 K. Once at 1133 K, the samples were maintained at this temperature for 5 h, then were cooled down to room temperature at a rate of 2 K/min.

## 2.2 Samples characterization

The structure and phase characteristics were determined using the X-ray powder diffraction method on a Bruker D8 focus diffractometer with  $\text{CuK}\alpha$  radiation ( $\lambda = 1.5406 \text{ \AA}$ ) at  $15^\circ \leq 2\theta \leq 80^\circ$ . Scanning electron microscope (SEM) micrographs were taken with an AIS 2100C microscope at 20 kV and a resolution of 5 m. The chemical composition of the samples was determined using energy-dispersive X-ray analysis (EDX) with a detector-type SDD Apollo X accelerated at 20 kV. The X-ray photoelectron spectroscopy (XPS) investigation was carried out on the surface of the samples using a KRATOS X SAM 800 spectrometer to obtain important quantitative and chemical condition data. The standard four-probe technique was used to measure resistivity curves, and liquid nitrogen was used to reduce the temperature from 269 to 77 K. Using  $I$ - $V$  curves at liquid nitrogen temperature (77 K), the critical current density  $J_c$  was calculated.

## 3 Results and discussion

### 3.1 X-ray powder diffraction (XRD)

X-ray powder diffraction patterns for  $\text{Tl}_{0.8}\text{Hg}_{0.2}\text{Ba}_2\text{Ca}_{2-x}\text{R}_x\text{Cu}_3\text{O}_{9-\delta-y}\text{F}_y$ , where  $R=\text{Sm}$  and  $\text{La}$   $x = 0.00, 0.025, 0.050, 0.075, \text{ and } 0.10$  are shown in Figs. 1a, b. By referring to the ICDD entry of the Tl-1223 superconducting phase (ICDD card #44-0476), in both substitutions, the majority of peaks belong to the tetragonal structure of (Tl, Hg)-1223 phase with a space group  $\text{P4/mmm}$  [18, 25]. Moreover, low-intensity minor peaks were assigned to the existence of secondary impurity phases, such as (Tl, Hg)-1212 phase,  $\text{BaHgO}_2$ ,  $\text{BaCuO}_2$ , and  $\text{CaHgO}_2$  usually formed in the single-step solid-state reaction [29]. Impurities such as  $\text{BaCuO}_2$  have decomposition temperatures of more than 1100  $^\circ\text{C}$  and cannot be removed from superconducting samples unless the material is heated above this temperature [30]. It's important

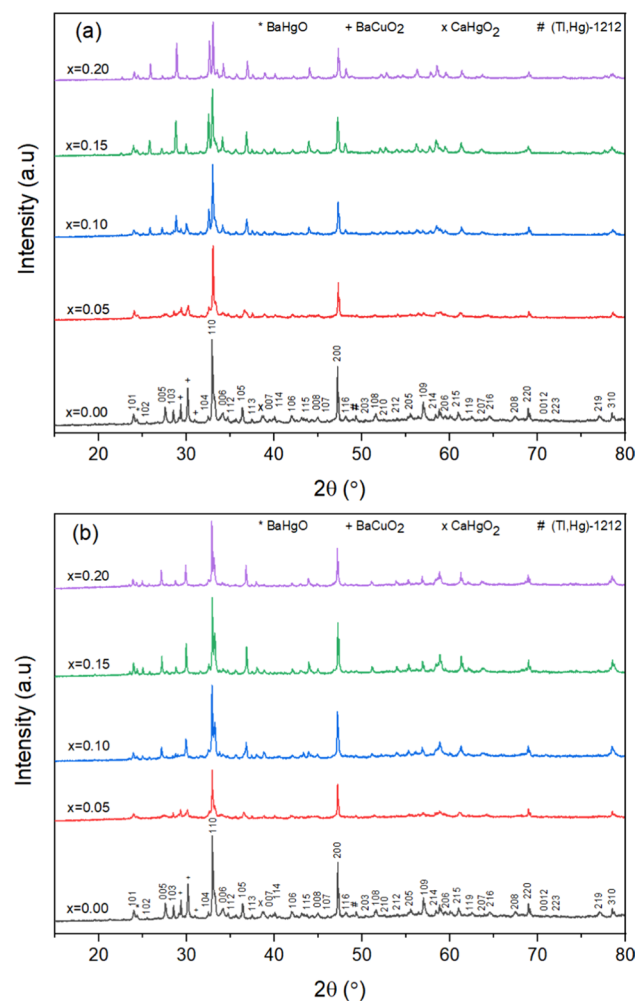


**Fig. 1** XRD patterns for  $\text{Tl}_{0.8}\text{Hg}_{0.2}\text{Ba}_2\text{Ca}_{2-x}\text{R}_x\text{Cu}_3\text{O}_{9-\delta-y}\text{F}_y$  superconducting phase for (a)  $R=\text{Sm}$  and (b)  $R=\text{La}$

to note that both the Sm and La replacements retain the tetragonal structure since they do not affect Bragg's diffraction peak positions. This is demonstrated by the similarity of the X-ray pattern and the execution of the Rietveld refinement for all the produced specimens using the MAUD software as shown in Fig. 2a–c of  $\text{Tl}_{0.6}\text{Hg}_{0.2}\text{Ba}_2\text{Ca}_2\text{Cu}_3\text{O}_{9-\delta}$ ,  $\text{Tl}_{0.8}\text{Hg}_{0.2}\text{Ba}_2\text{Ca}_{1.9}\text{Sm}_{0.1}\text{Cu}_3\text{O}_{9-\delta-y}\text{F}_y$ , and  $\text{Tl}_{0.8}\text{Hg}_{0.2}\text{Ba}_2\text{Ca}_{1.9}\text{La}_{0.1}\text{Cu}_3\text{O}_{9-\delta-y}\text{F}_y$ , respectively [31]. The results of the refinement analysis showed that the measured and calculated patterns had a satisfyingly great match in peak fitting. Their refinement parameters were used as the numerical criteria for fitting, such as the profile residual reliability factor ( $R_p$ ), weighted profile residual factor ( $R_{wp}$ ), expected weighted profile factor ( $R_{exp}$ ), and goodness of fit parameters ( $\chi^2$ ), the values of which are listed in Table 1. Using the Rietveld refinement, the relative volume fractions of (Tl, Hg)-1223, (Tl, Hg)-1212,  $\text{BaHgO}_2$ ,  $\text{BaCuO}_2$ , and  $\text{CaHgO}_2$  were determined and listed in Table 1. The

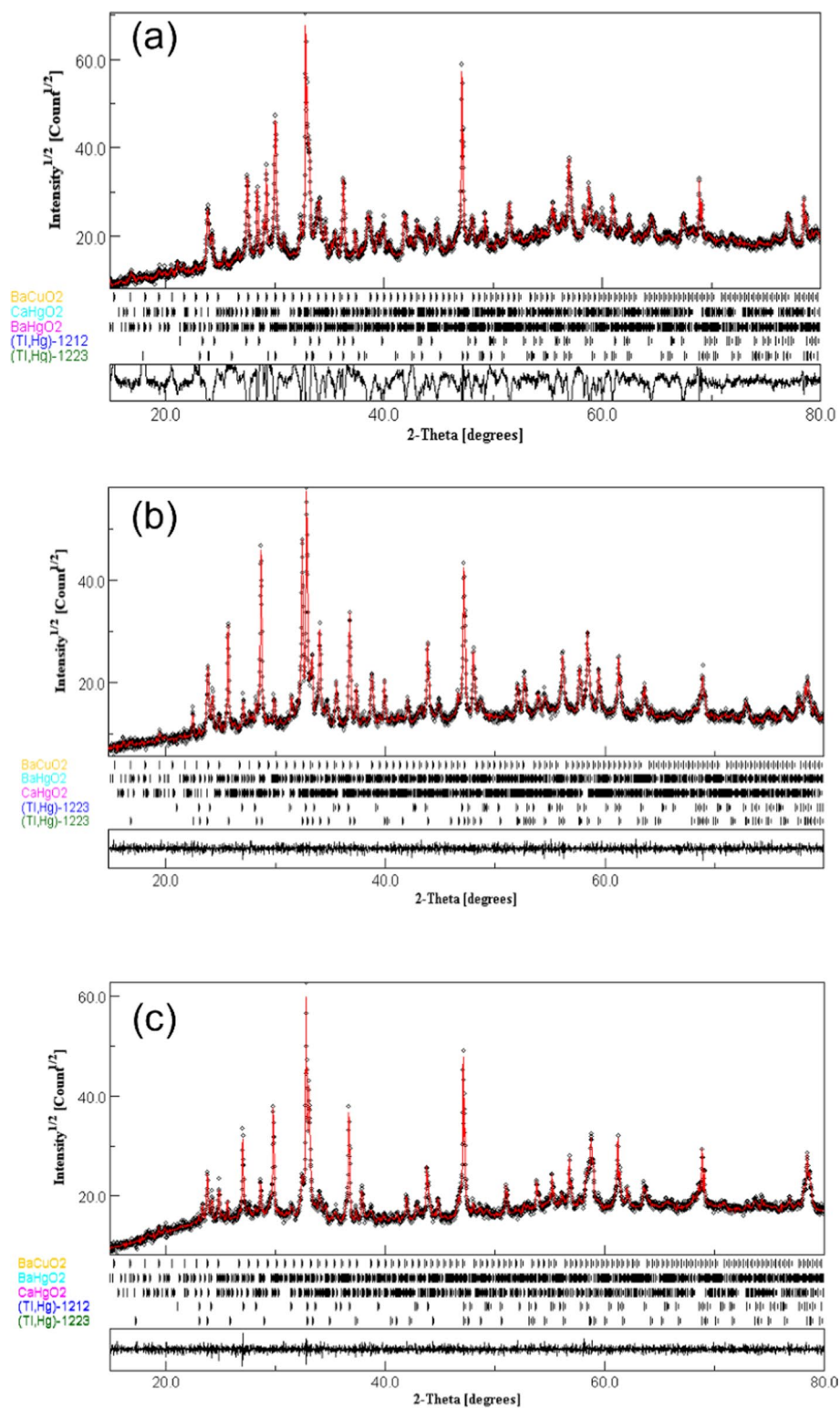


**Fig. 2** Rietveld refinements of the XRD spectra of (a)  $\text{Tl}_{0.6}\text{Hg}_{0.2}\text{Ba}_2\text{Ca}_2\text{Cu}_3\text{O}_{9-\delta}$ , (b)  $\text{Tl}_{0.8}\text{Hg}_{0.2}\text{Ba}_2\text{Ca}_{1.9}\text{Sm}_{0.1}\text{Cu}_3\text{O}_{9-\delta-y}\text{F}_y$ , and (c)  $\text{Tl}_{0.8}\text{Hg}_{0.2}\text{Ba}_2\text{Ca}_{1.9}\text{La}_{0.1}\text{Cu}_3\text{O}_{9-\delta-y}\text{F}_y$

**Table 1** Variation of volume fractions, structural and refinement parameters for  $\text{Tl}_{0.8}\text{Hg}_{0.2}\text{Ba}_2\text{Ca}_{2-x}\text{R}_x\text{Cu}_3\text{O}_{9-\delta-y}\text{F}_y$  samples with  $x = 0.00, 0.025, 0.050, 0.075, \text{ and } 0.10$  for  $\text{R} = \text{Sm}$  and  $\text{La}$ 

x	Volume fraction %					Unit cell parameters		Refinement Parameters			
	(Tl, Hg)-1223	(Tl, Hg)-1212	CaHgO <sub>2</sub>	BaHgO <sub>2</sub>	BaCuO <sub>2</sub>	a (Å)	c (Å)	$\chi^2$	$R_{wp}$	$R_{exp}$	$R_p$
0.000	75.95	3.98	0.37	1.35	18.32	3.843	15.85	1.09	2.66	2.44	0.019
Sm Substitution											
0.025	90.93	1.15	1.49	1.33	5.08	3.843	15.84	1.37	2.91	2.12	0.029
0.050	91.10	0.79	0.91	0.85	5.58	3.844	15.83	1.42	2.88	2.02	0.027
0.075	90.48	0.81	0.99	0.95	8.92	3.845	15.82	1.51	2.82	1.87	0.023
0.100	90.71	0.83	1.06	1.7	9.30	3.846	15.80	1.48	3.01	2.03	0.025
La Substitution											
0.025	92.37	1.49	1.36	1.35	3.45	3.846	15.84	1.24	2.65	2.13	0.020
0.050	86.17	4.31	2.41	1.69	5.41	3.848	15.83	1.18	2.64	2.23	0.028
0.075	84.20	1.36	2.42	1.15	1.19	3.851	15.79	1.03	2.71	2.61	0.025
0.100	83.61	0.55	1.97	2.58	5.99	3.852	15.78	1.07	2.75	2.57	0.026

(Tl, Hg)-1223 volume fractions of the substituted samples were found to be greater than those of the pure sample in both substitutions. In Sm substitution, the main phase's volume fraction percentage gradually increases from 75.95% to 91.10%, indicating a 19.95% increase as  $x$  increases from 0.00 to 0.05. Similarly, in the case of La substitution, the volume fraction of the main phase increases to 92.37%, with a rate of 21.62% as  $x$  increases to 0.025. This suggests that  $\text{LaF}_3$  replacement has a greater impact on the formation of the (Tl, Hg)-1223 superconductor phase than  $\text{SmF}_3$ . The electronic configuration and valence state of the substituting ion can affect the phase formation process.  $\text{Sm}^{3+}$  and  $\text{La}^{3+}$  possess dissimilar electronic structures, and this divergence in electronic behavior can impact the bonding interactions within the crystal lattice, potentially resulting in a higher tendency for phase formation. Additionally, several peaks showed an increase in intensity with Sm substitution; this may be explained by the possibility that the substitution of  $\text{Sm}^{3+}$  ions may encourage improved crystal lattice ordering in the superconductor [32]. More constructive interference between X-rays and crystal planes can be produced by improved ordering, increasing the strength of some diffraction peaks in the XRD spectrum. As the Sm and La contents increase, the lattice parameter  $a$  elongates. This elongation is most likely caused by electron addition into the antibonding orbital caused by partial substitution of  $\text{Ca}^{2+}$  ions by  $\text{Sm}^{3+}$  and  $\text{La}^{3+}$  ions [17]. Moreover, with increasing Sm and La concentrations, the elongation rate of  $a$  is predicted to be  $(da/dx) = 0.03$  and  $0.09$ , respectively. The elongation with La substitution is clearly higher than that with Sm replacement. This may be attributed to variations in ionic size, chemical interactions, electronic configuration, local effects, and crystal symmetry between these two ions. In contrast, when Sm and La content increases,  $c$  decreases. This decrease is

thought to be caused by the fact that the ionic radii of  $\text{Sm}^{3+}$  (0.96 Å) and  $\text{La}^{3+}$  (1.03 Å) are less than those of  $\text{Ca}^{2+}$  ions (1.12 Å) [30, 31]. The contraction rate of  $c$  is estimated to be  $(dc/dx) = -0.48$  and  $-0.76$  as Sm and La contents increase, respectively. The higher ionic radius of  $\text{La}^{3+}$  may cause a bigger deformation of the crystal lattice when  $\text{La}^{3+}$  is substituted for  $\text{Ca}^{2+}$  than  $\text{Sm}^{3+}$  substitution in the superconductor lattice. The lattice parameter  $c$  may fall more noticeably because of this bigger distortion. Additionally, an increase in fluorine might be the cause of the decrease in the lattice parameter  $c$ . This is caused by two potential factors: first, fluorine has a little smaller ionic radius (1.47 Å) than oxygen (1.52 Å), and second, fluorine has a higher electronegativity (3.98) than oxygen (3.44) [23].

### 3.2 Size, surface morphology, and elemental compositions

Figures 3 and 4 show the respective SEM micrographs of  $\text{Tl}_{0.8}\text{Hg}_{0.2}\text{Ba}_2\text{Ca}_{2-x}\text{R}_x\text{Cu}_3\text{O}_{9-\delta-y}\text{F}_y$  and  $\text{Tl}_{0.8}\text{Hg}_{0.2}\text{Ba}_2\text{Ca}_{2-x}\text{La}_x\text{Cu}_3\text{O}_{9-\delta}$ , with  $x = 0.00, 0.025, 0.050, 0.075, \text{ and } 0.10$ . The presence of rectangular plates in the morphologies indicates the formation of the (Tl, Hg)-1223 phase [16, 33]. Additionally, the irregular shapes found inside the grains are related to non-superconducting phases and impurity phases like (Tl, Hg)-1212, as depicted in XRD results. It is worth noting that the rectangular shape remains consistent as substitution content increases. The low substitution of Sm and La with  $x = 0.025$ , on the other hand, promotes the growth of the (Tl, Hg)-1223 plates, improves their alignments, and reduces porosity among the superconducting grains. As the substitution contents of Sm and La increase, the number of irregular shapes and porosity also increases, as evident in Figs. 3 and 4c–e. Similar results

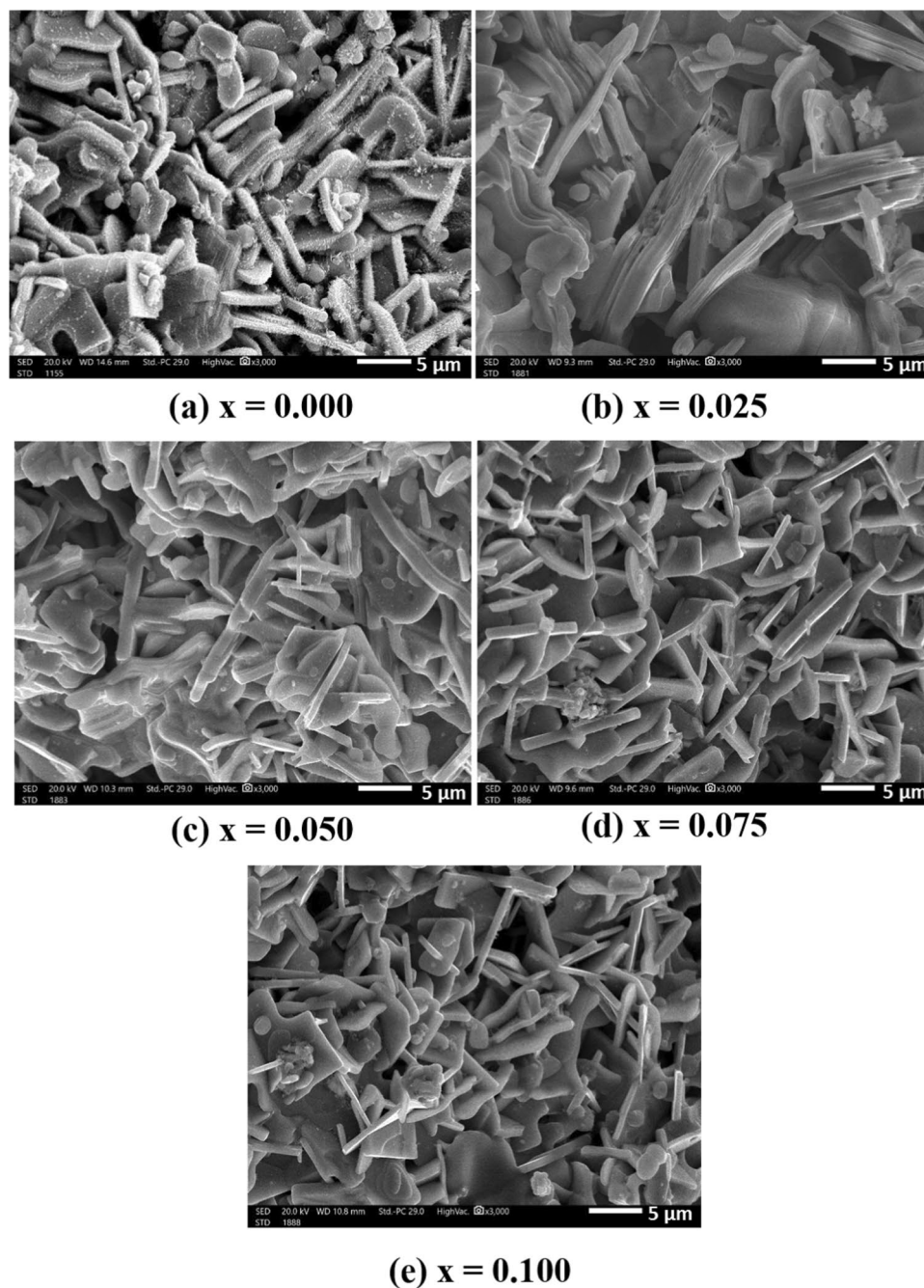


**Fig. 3** SEM micrographs of  $\text{Tl}_{0.8}\text{Hg}_{0.2}\text{Ba}_2\text{Ca}_{2-x}\text{Sm}_x\text{Cu}_3\text{O}_{9-\delta-y}\text{F}_y$  with (a)  $x = 0.000$ , (b)  $x = 0.025$ , (c)  $x = 0.050$ , (d)  $x = 0.075$ , and (e)  $x = 0.100$

were observed in  $\text{La}^{3+}$ ,  $\text{Pr}^{3+}$ , and  $\text{Sc}^{3+}$  doped phases at the Ca site in Tl-1223 and  $(\text{Cu}_{0.5}\text{Tl}_{0.5})$ -1223 phases [15, 28]. As a result, low Sm and La substitution contents enhance the rate formation the of (Tl, Hg)-1223 superconductor phase.

To confirm the existence of the  $\text{Tl}_{0.8}\text{Hg}_{0.2}\text{Ba}_2\text{Ca}_{2-x}\text{R}_x\text{Cu}_3\text{O}_{9-\delta-y}\text{F}_y$  phase, where  $\text{R} = \text{Sm}$  and  $\text{La}$ , a certain number of grains are randomly examined by EDX. EDX spectra for  $\text{Tl}_{0.8}\text{Hg}_{0.2}\text{Ba}_2\text{Ca}_2\text{Cu}_3\text{O}_{9-\delta}$ ,

$\text{Tl}_{0.8}\text{Hg}_{0.2}\text{Ba}_2\text{Ca}_{1.9}\text{Sm}_{0.1}\text{Cu}_3\text{O}_{9-\delta-y}\text{F}_y$ , and  $\text{Tl}_{0.8}\text{Hg}_{0.2}\text{Ba}_2\text{Ca}_{1.9}\text{La}_{0.1}\text{Cu}_3\text{O}_{9-\delta-y}\text{F}_y$  grains in two distinct regions are shown in Figs. 5a, b, c, respectively. The corresponding atomic percentages of the elements present in these grains are listed in Table 2.

The EDX spectra for all samples demonstrated that the positions of the Tl, Hg, Ba, Ca, O, and Cu peaks stay unchanged, whereas the peak for Sm and La appeared when

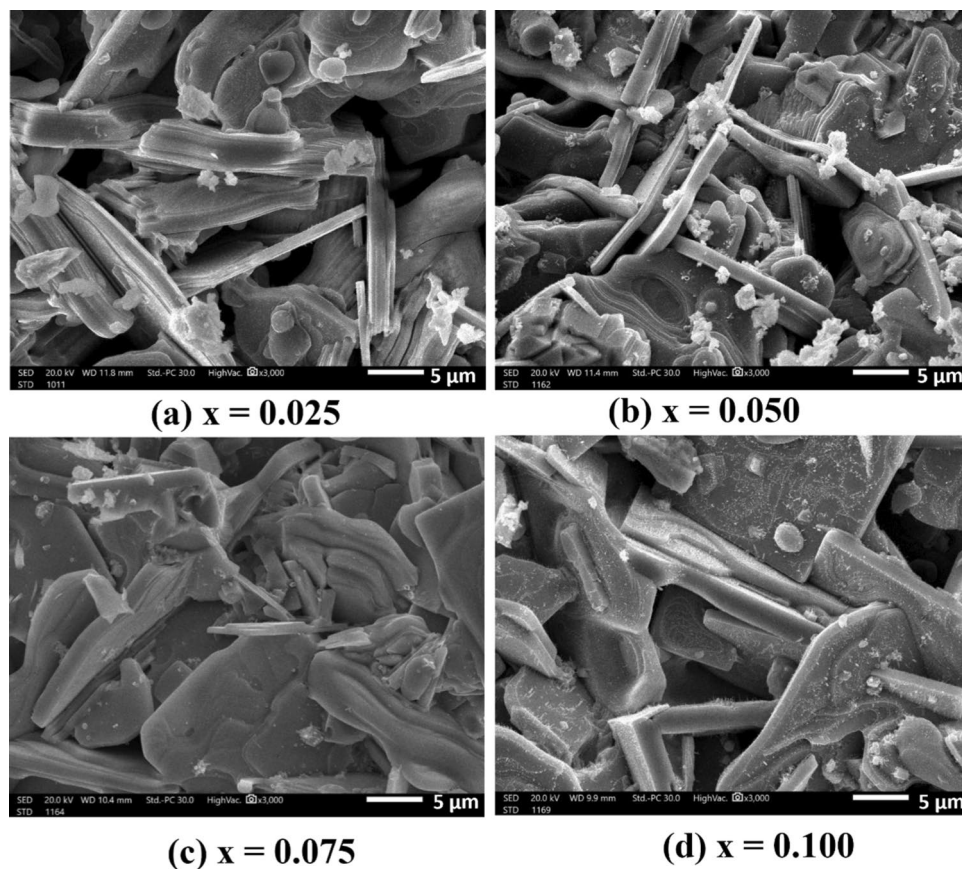


**Fig. 4** SEM micrographs of  $\text{Tl}_{0.8}\text{Hg}_{0.2}\text{Ba}_2\text{Ca}_{2-x}\text{La}_x\text{Cu}_3\text{O}_{9-\delta-y}\text{F}_y$  with (a)  $x = 0.025$ , (b)  $x = 0.050$ , (c)  $x = 0.075$ , and (d)  $x = 0.100$

$\text{Sm}^{3+}$  and  $\text{La}^{3+}$  ions are substituted in the position of  $\text{Ca}^{2+}$  ions, and the peak for F occurred when substituted for O. Moreover, the positions and intensities of the peaks exhibit consistency across the two regions, indicating the high homogeneity in the examined samples. These results suggest that Sm and La are effectively substituted in the (Tl, Hg)-1223 microstructure. Furthermore, the atomic percentages of Ca, Sm, La, O, and F in both replacements are shown in Figs. 6 and 7. The results clearly illustrate that when  $x$  increases, the replacement of Ca and O is done with (Sm, La) and F, respectively. A decrease in calcium and oxygen atomic percentages is observed along with a rise in Sm, La, and F atomic percentages.

### 3.3 X-ray photoelectron spectroscopy (XPS)

To validate the XRD findings and identify the oxidation states of various elements in  $\text{Tl}_{0.8}\text{Hg}_{0.2}\text{Ba}_2\text{Ca}_{2-x}\text{Sm}_x\text{Cu}_3\text{O}_{9-\delta-y}\text{F}_y$  and  $\text{Tl}_{0.8}\text{Hg}_{0.2}\text{Ba}_2\text{Ca}_{2-x}\text{La}_x\text{Cu}_3\text{O}_{9-\delta-y}\text{F}_y$ , with  $x = 0.00, 0.025, 0.050, 0.075$ , and  $0.10$ , XPS analysis was performed. Figure 8a, b shows the survey spectra for both substitutions. The pure sample's survey spectrum ( $x = 0.00$ ) revealed the presence of thallium (Tl), Mercury (Hg) barium

(Ba), calcium (Ca), copper (Cu), oxygen (O), and traces of carbon (C), due to the sample's contact with outside air before the XPS analysis [37]. The presence of Lanthanum (La) and Samarium (Sm), in addition to the main elements, is observable in the survey spectra of the substituted samples.

Studies on oxide superconductor interfaces have focused heavily on the impact of metal atoms on Cu–O bonds [38]. Figure 9a, b depicts the oxidation state of Cu for all samples, which reveals the existence of copper ( $\text{Cu}2p$ ). In both substitutions, the primary peak at 934 eV and the satellite peak at 942.5 eV is  $\text{Cu}2p_{3/2}$ , whereas the following two peaks are  $\text{Cu}2p_{1/2}$  [39]. Moreover, in Fig. 12a, the peak positions of  $\text{Cu}2p_{3/2}$  and  $\text{Cu}2p_{1/2}$  in the (Tl, Hg)-1223 superconducting phase are depicted as a function of Sm and La contents  $x$ . The observed shifts in these peaks with increasing doping levels provide crucial insights into the alterations in the chemical environment and electronic structure of copper within the (Tl, Hg)-1223 lattice. The satellite peaks are caused by the "shake-up" process, which happens when excess electrons are stimulated to higher energy levels [40]. The Cu–O spectra published previously [38] were obviously compatible with the  $\text{Cu}2p_{3/2}$  and  $\text{Cu}2p_{1/2}$  peaks, which are separated by roughly 20 eV. According to XPS investigation,

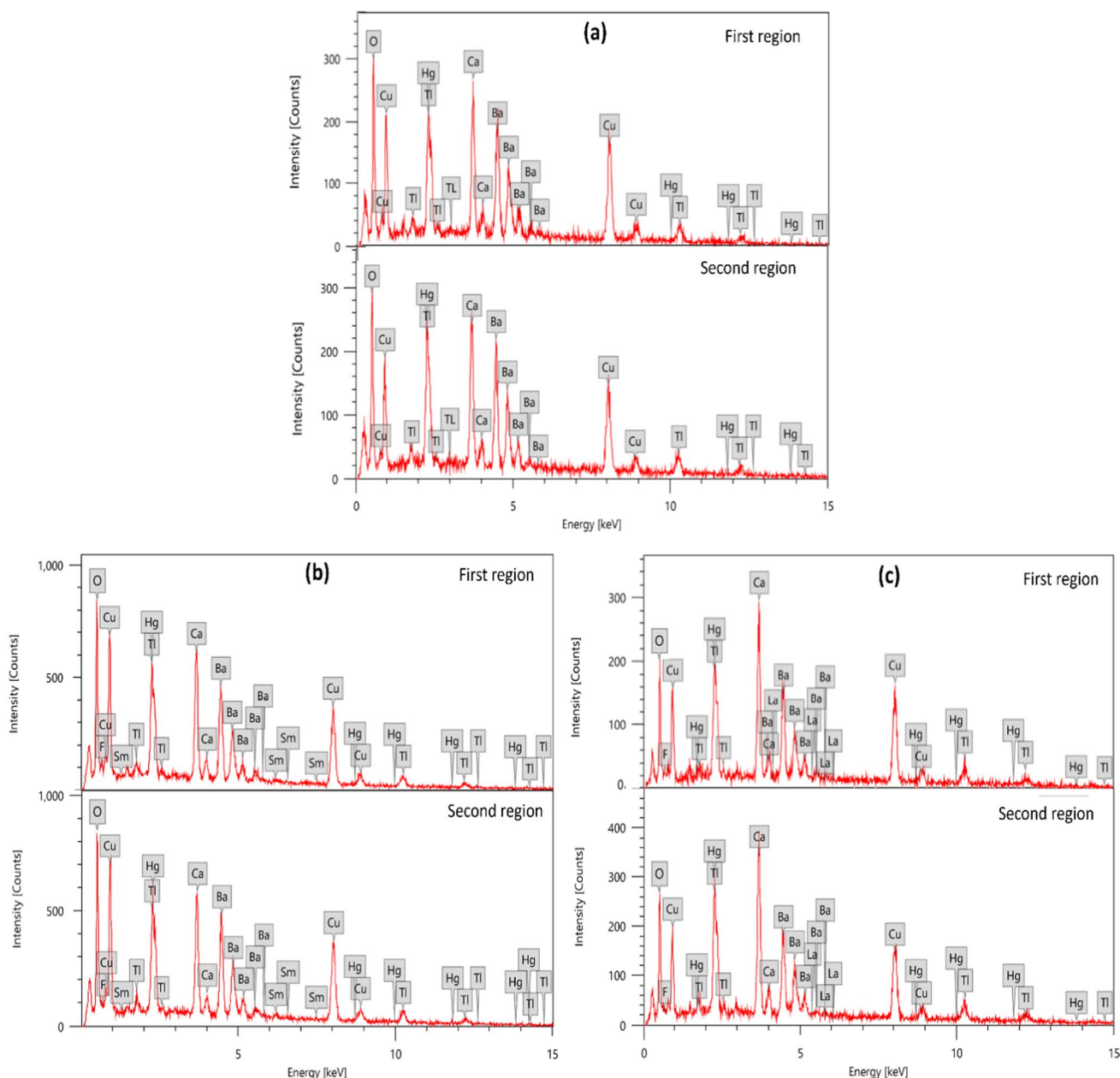


**Fig. 5** EDX spectra of (a)  $\text{Tl}_{0.8}\text{Hg}_{0.2}\text{Ba}_2\text{Ca}_2\text{Cu}_3\text{O}_{9-\delta}$ , (b)  $\text{Tl}_{0.8}\text{Hg}_{0.2}\text{Ba}_2\text{Ca}_{1.9}\text{Sm}_{0.1}\text{Cu}_3\text{O}_{9-\delta-y}\text{F}_y$ , and (c)  $\text{Tl}_{0.8}\text{Hg}_{0.2}\text{Ba}_2\text{Ca}_{1.9}\text{La}_{0.1}\text{Cu}_3\text{O}_{9-\delta-y}\text{F}_y$

the majority of conduction in Cu–O occurs through the hopping of holes between  $\text{Cu}^{2+}$  and  $\text{Cu}^{3+}$ , which causes the formation of grain boundaries [29].

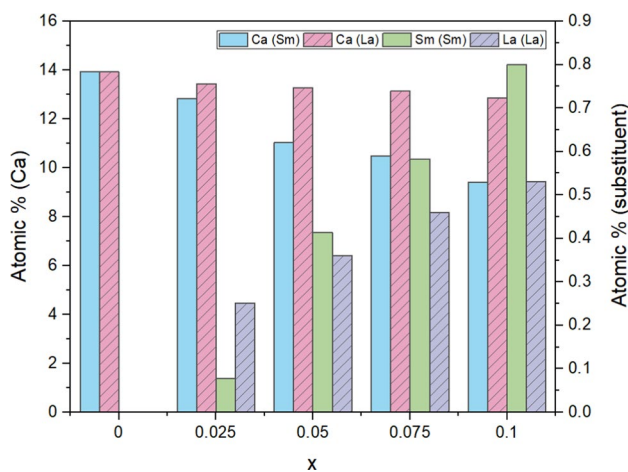
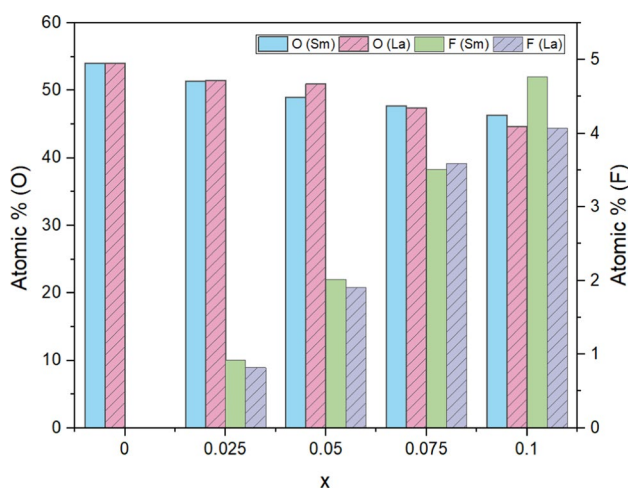
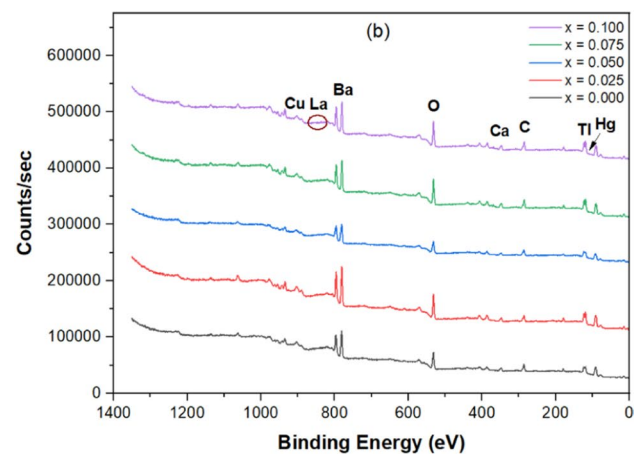
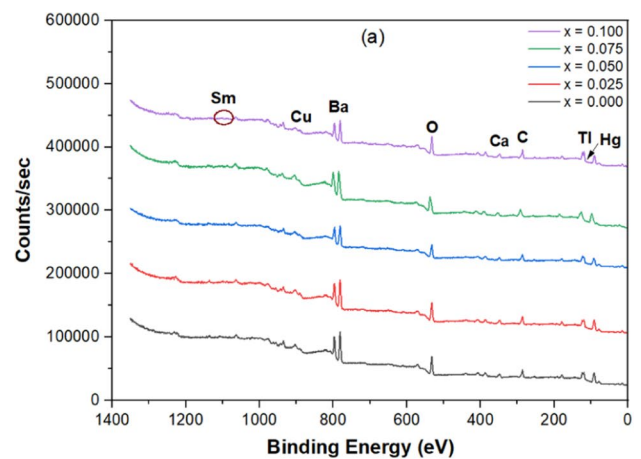
Figure 10a, b shows high-resolution XPS spectra of Ca 2p for all superconducting samples, as well as the corresponding deconvoluted spectra. Ca has a relatively stable 2+ oxidation state, where the  $2p_{1/2}$ , and  $2p_{3/2}$  doublets have a binding energy gap of 3.66 eV [41]. However, the replacement of Sm and La in the samples affects the oxidation states of calcium and the shift in the binding energy, as illustrated in Fig. 12b.

Figure 11a displays the Sm 3d XPS spectra of  $\text{Tl}_{0.8}\text{Hg}_{0.2}\text{Ba}_2\text{Ca}_{2-x}\text{Sm}_x\text{Cu}_3\text{O}_{9-\delta-y}\text{F}_y$  ( $x = 0.025, 0.050, 0.075,$  and  $0.100$ ).  $\text{Sm}3d_{5/2}$  and  $\text{Sm}3d_{3/2}$ , with binding energies of 1083 eV and 1109.2 eV, respectively, are represented by the two major peaks [42]. These results confirm that Sm ions were present in the Sm substituted samples as  $\text{Sm}^{3+}$  [43]. Figure 11b shows the La 3d spectra of  $\text{Tl}_{0.8}\text{Hg}_{0.2}\text{Ba}_2\text{Ca}_{2-x}\text{La}_x\text{Cu}_3\text{O}_{9-\delta-y}\text{F}_y$  ( $x = 0.025, 0.050, 0.075,$  and  $0.100$ ) with two distinct peaks at 836.7 and 848.4 eV. The peak at 836 is attributed to  $\text{La} 3d_{5/2}$ , while the peak at 848 is attributed to  $\text{La} 3d_{3/2}$  [44]. All of the La replaced



**Table 2** The atomic percentage of the elemental composition analysis by EDX of  $Tl_{0.8}Hg_{0.2}Ba_2Ca_{2-x}R_xCu_3O_{9-\delta-y}F_y$  superconducting phase

	Atomic %					
	$x = 0.00$		$x = 0.10$ (Sm Substitution)		$x = 0.10$ (La Substitution)	
	First Region	Second Region	First Region	Second Region	First Region	Second Region
O	54.02	53.28	48.87	48.38	46.67	47.50
F			4.56	4.77	4.50	4.10
Ca	13.93	13.91	11.51	9.42	12.24	12.80
Cu	16.46	16.80	17.20	18.31	18.30	17.99
Ba	10.29	10.31	11.40	12.70	11.60	11.41
R			0.80	0.79	0.57	0.53
Hg	0.90	1.10	0.98	1.10	1.20	1.00
Tl	4.40	4.60	4.68	4.53	4.92	4.67

**Fig. 6** The variation of atomic percentage with  $x$  of Ca, Sm, and La for  $Tl_{0.8}Hg_{0.2}Ba_2Ca_{2-x}R_xCu_3O_{9-\delta-y}F_y$  superconducting phase, where  $R = Sm$  and La**Fig. 7** The variation of atomic percentage with  $x$  of O and F for  $Tl_{0.8}Hg_{0.2}Ba_2Ca_{2-x}R_xCu_3O_{9-\delta-y}F_y$  superconducting phase, where  $R = Sm$  and La**Fig. 8** XPS spectra of the  $Tl_{0.8}Hg_{0.2}Ba_2Ca_{2-x}R_xCu_3O_{9-\delta-y}F_y$  superconductor phase for  $x = 0.00, 0.025, 0.05, 0.075,$  and  $0.10$  for (a)  $R = Sm$  and (b)  $R = La$ 

samples' findings corroborate the occurrence of La in the  $La^{3+}$  state [45]. Notably, Figs. 12c, d further reveal the shifts between the two main peaks in the Sm and La spectra, providing additional insights into the alterations

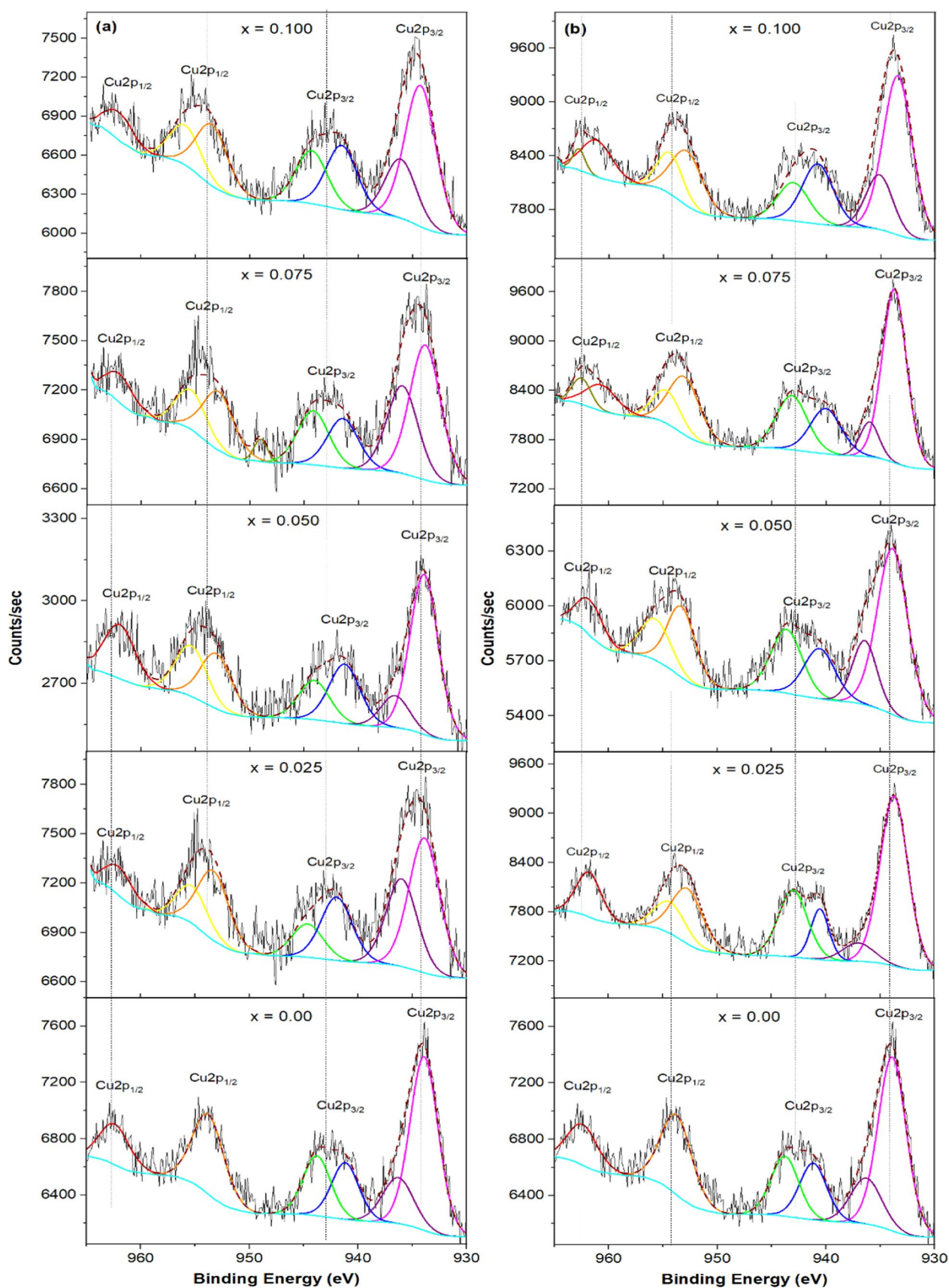


Fig. 9 Deconvoluted XPS spectra of Cu<sub>2</sub>p for (a) Sm substitution and (b) La substitution

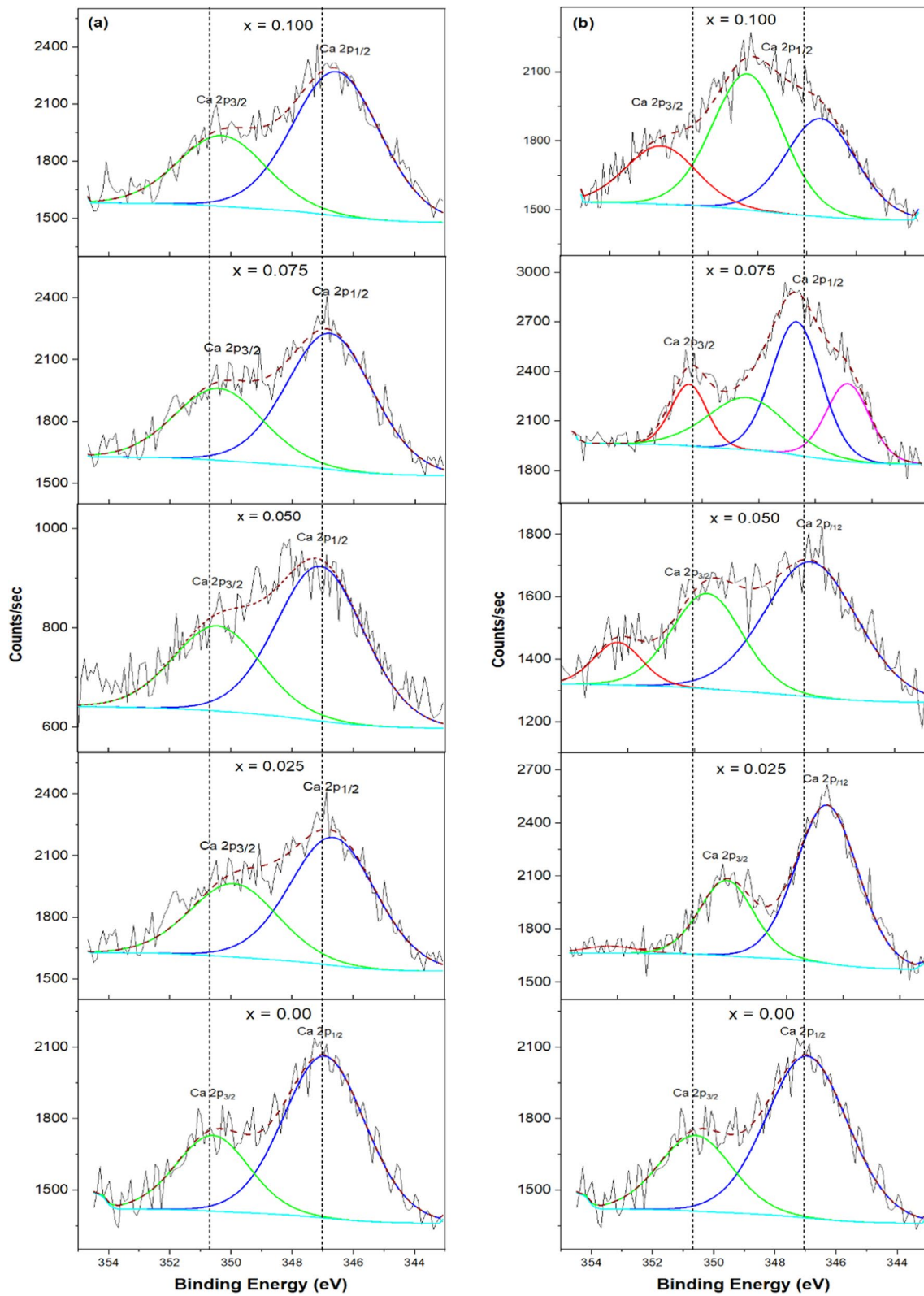
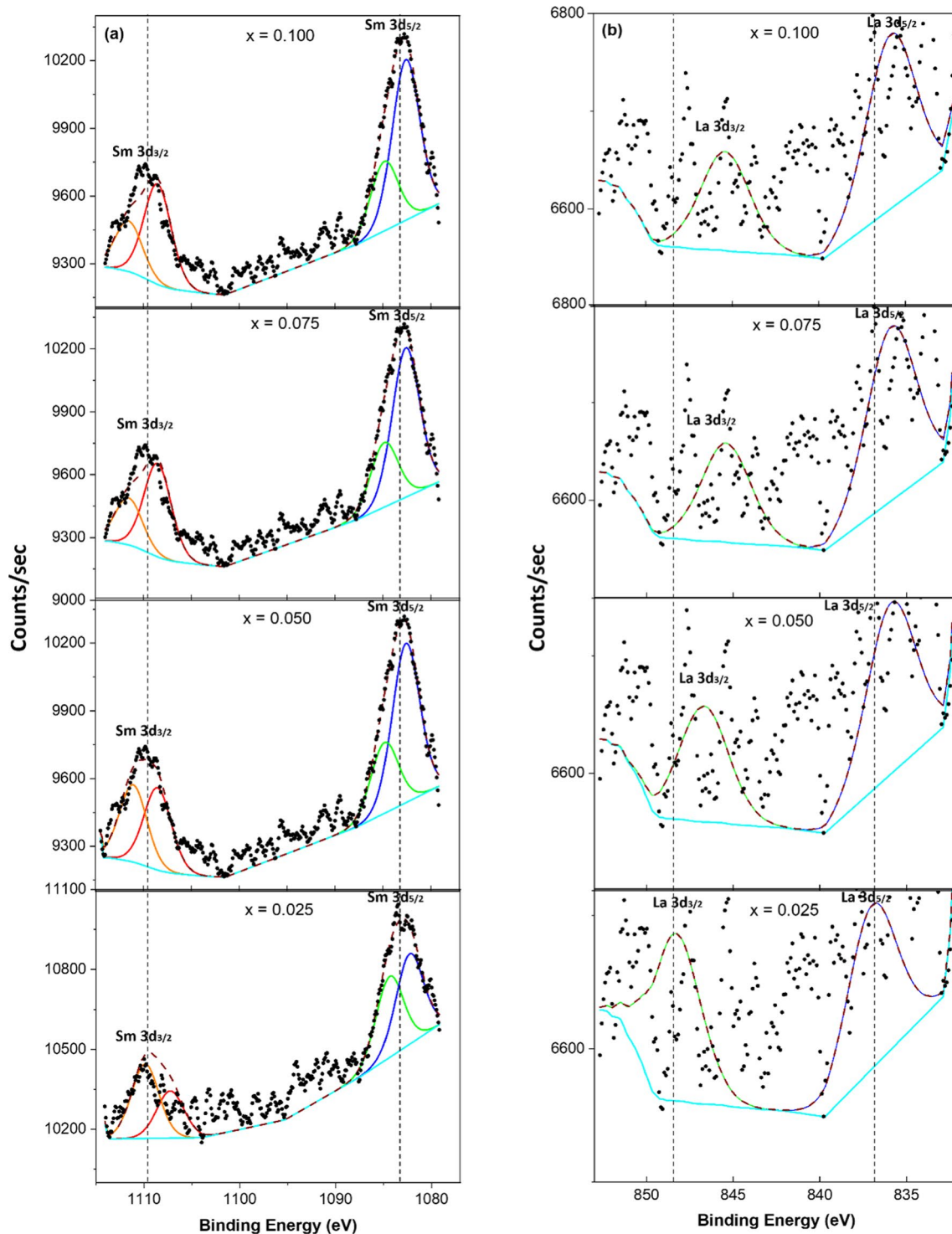


Fig. 10 Deconvoluted XPS spectra of Ca<sub>2p</sub> for (Tl, Hg)-1223 phase: (a) Sm substitution and (b) La substitution



**Fig. 11** Deconvoluted XPS spectra for (Tl, Hg)-1223 phase of: (a) Sm3d and (b) La3d

induced by these dopants in the (Tl, Hg)-1223 superconducting phase. Moreover, the weak-photoemission cross section at the excitation energy employed results in noisy La 3d XPS spectra [46].

### 3.4 Electrical resistivity measurements

The temperature-dependent of resistivity measurements for  $\text{Tl}_{0.8}\text{Hg}_{0.2}\text{Ba}_2\text{Ca}_{2-x}\text{R}_x\text{Cu}_3\text{O}_{9-\delta-y}\text{F}_y$  phase, where  $R = \text{Sm}$

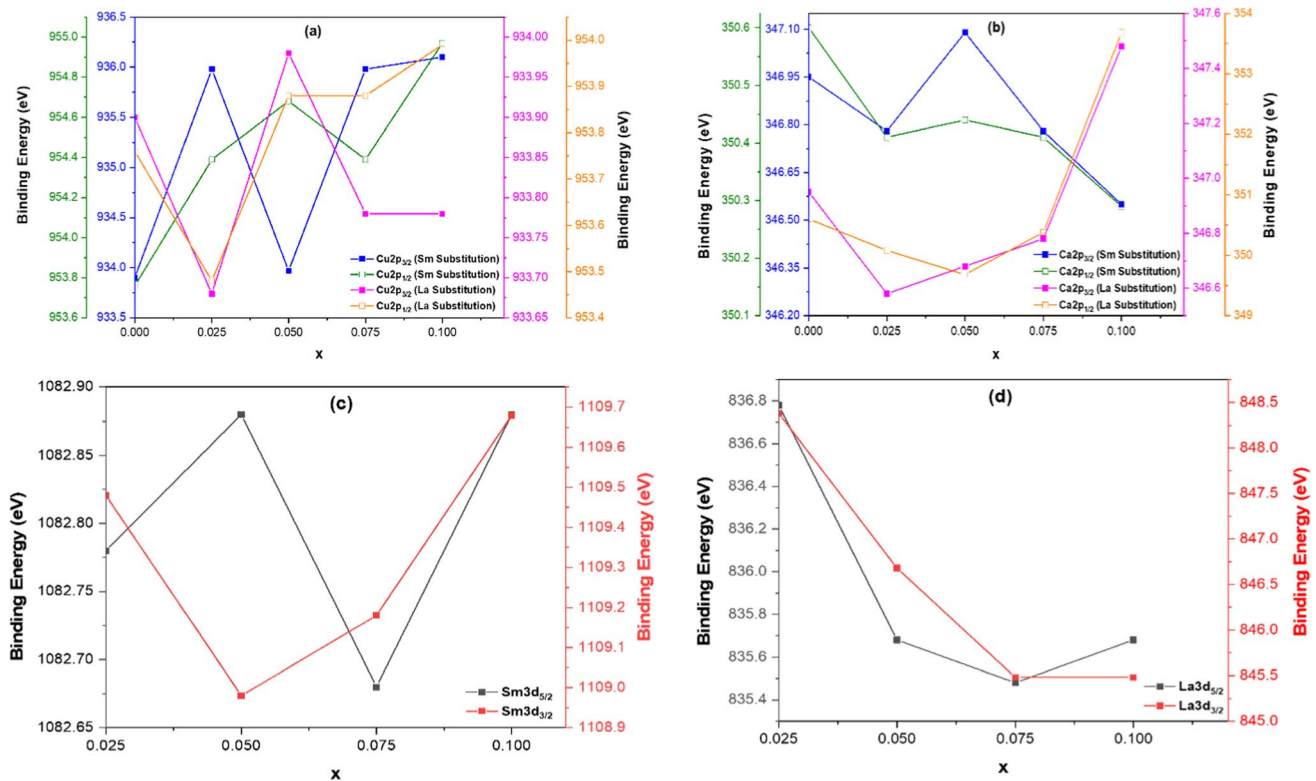


**Fig. 12** Variation in the main peaks' binding energies with dopant content  $x$  in (Tl, Hg)-1223 superconducting phase of: (a) Cu2p, (b) Ca2p, (c) Sm3d, and (d) La3d

and La with  $x = 0.00, 0.025, 0.050, 0.075,$  and  $0.10$  are shown in Figs. 13a, b, respectively. The measurements were conducted over a temperature range from room temperature down to zero-resistivity temperature  $T_0$ . According to the figures, from the room temperature down to the pseudogap temperature  $T^*$ , which is the point at which  $((\rho_m(T) - \rho_0)/\alpha T)$  deviates from 1, all the samples showed metallic variation, which was followed by the superconducting transition at lower temperatures. Below  $T^*$ , the resistivity curve increasingly departed from linear behavior, followed by notable rounding, which appears to be driven by conductivity variations corresponding to the pseudo gap opening [47]. When the temperature falls below  $T^*$ , a few electron pairs form. These electron pairs do not have the long-range coherence required for superconductivity. As the temperature drops, the number of generated electron pairs increases until it approaches  $T_c$ , at which point all conducting electrons are paired and behave in a correlated manner [31]. Once  $T_c$  is attained, the resistivity curves rapidly decrease until the  $T_0$  is reached.  $T_c$  is estimated from the first-order derivative peak  $(dp(T)/dT)$ , as shown in the inset of Figs. 13 (a and b) and  $T_0$  is the temperature at zero electrical resistivity. The values of  $T_c$ ,  $T_0$ , and  $T^*$  are tabulated in Table 3. All of the samples exhibit practically a single peak at

$T_c$ , confirming a transition within the superconducting grains [48]. According to Table 3 and Figs. 13a, b,  $T_c$  increases from 105.4 K to 112.0 K at a rate of 6.26% for Sm substitutions and 116.4 K at a rate of 10.72% for La substitutions as  $x$  changes from 0.00 to 0.025, then  $T_c$  falls as  $x$  increases further. Subsequently,  $T_c$  decreases to 99.9 K at a decreasing rate of 10.80% for Sm substitution and to 105.7 K at a decreasing rate of 9.85% for La substitution as  $x$  is further increased to  $x = 0.1$ . Additionally,  $T_0$  exhibits the same behavior as  $T_c$  with Sm and La content. As a result, substituting Sm and La at the optimal content ( $x = 0.025$ ) enhances the superconducting transition temperature of the (Tl, Hg)-1223 phase. The increase in  $T_c$  and  $T_0$  up to  $x = 0.025$  in both replacements might be attributed to the decrease in weak connections between grains, as revealed by SEM micrographs [49]. Moreover, substituting  $\text{La}^{3+}$  is notably more effective in increasing  $T_c$ . This enhancement can be attributed to a higher volume fraction, as well as favorable ionic sizes and electronic structures, which are evident in XRD analysis. These combined factors foster an environment that facilitates more efficient formation of Cooper pairs, consequently resulting in the improved enhancement of  $T_c$ . Furthermore, the increase in  $T_c$  might be attributable to the reduction of the oxygen content caused by the substitution of

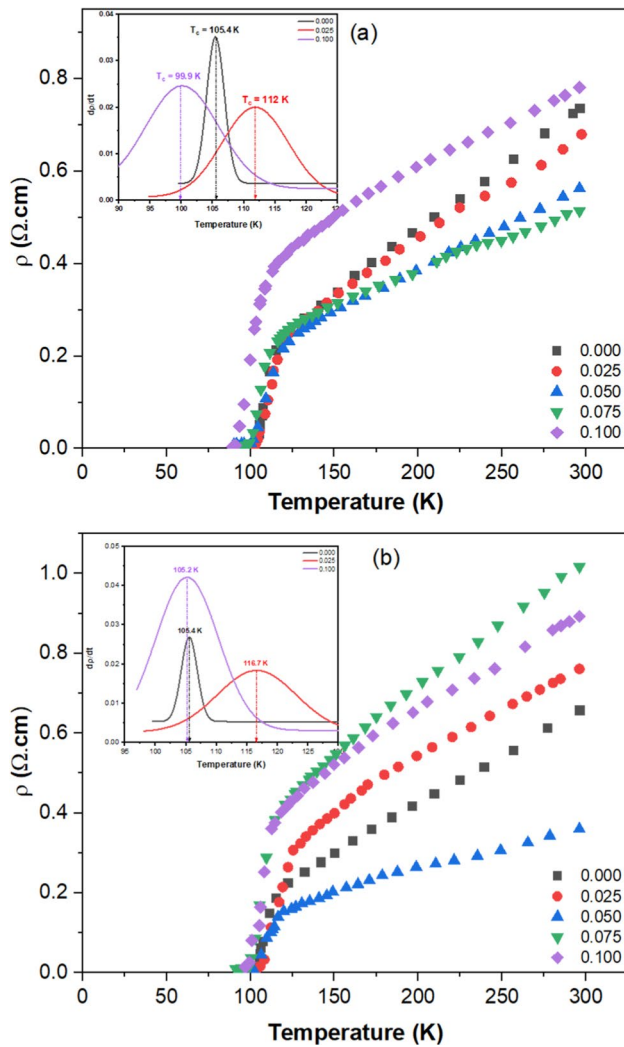


**Fig. 13** Variation of electrical resistivity as a function of temperature for  $\text{Tl}_{0.8}\text{Hg}_{0.2}\text{Ba}_2\text{Ca}_{2-x}\text{R}_x\text{Cu}_3\text{O}_{9-\delta-y}\text{F}_y$ ,  $0.00 \leq x \leq 0.10$ , superconducting samples: (a)  $R = \text{Sm}$  and (b)  $R = \text{La}$

O by F at  $x = 0.025$  as shown by EDX, which turns the samples from over-doped to optimally doped [23]. On the other hand, the gradual decrease in  $T_c$  for  $x > 0.025$  can be due to oxygen vacancy disorder and mobile carrier trapping [50]. Furthermore, the switch from optimally doped samples to under-doped samples may be the cause of the suppression in  $T_c$ , for  $x > 0.025$  [51]. There was no discernible trend for the values of  $T^*$  as Sm and La contents increased, as shown in Figs. 14a–c and Table 3. The findings demonstrated that for Sm and La replacement, respectively,  $x = 0.050$  and  $x = 0.025$  were related to the largest  $T^*$ .

The normal-state resistivity  $\rho_n(T)$  above  $T^*$  is described by the Matthiessen rule [42].

$$\rho_n(T) = \alpha T + \rho_0, \quad (1)$$

where  $\alpha$  represents the resistivity temperature coefficient and  $\rho_0$  stands for the residual resistivity. The values of the fitting parameters for  $\rho_0$ ,  $\alpha$ , the room-temperature resistivity  $\rho_{room}$ , and the superconducting transition width ( $\Delta T = T_c - T_0$ ) for all samples, were determined and listed in Table 3.  $\rho_0$  represents the defect density and homogeneity of the samples and is temperature independent. However,  $\alpha$  is a temperature-dependent intrinsic parameter that exhibits a small change with  $x$  due to the influence of  $\text{CuO}_2$  planes on charge carriers [52].  $\rho_{room}$  decreased up to  $x = 0.050$  for Sm substituted samples and up to  $x = 0.075$  for La-substituted samples then increased. This drop is ascribed to the Sm and La replacements, which reduce grain boundary resistance and improve inter-grain connectivity [24]. While an increase in  $\rho_{room}$  results from an increase in the number of scattering centers and diminishes inter-granular coupling [49]. The non-substituted sample had the smallest  $\Delta T$  (2.85 K) and ranged from 6 to 11 K for all substituted samples. This might be because

**Table 3** Variation of  $\alpha$ ,  $T_0$ ,  $T_c$ ,  $\Delta T$ ,  $\rho_0$ , and  $\rho_n$  for  $\text{Tl}_{0.8}\text{Hg}_{0.2}\text{Ba}_2\text{Ca}_{2-x}\text{R}_x\text{Cu}_3\text{O}_{9-\delta-y}\text{F}_y$ ,  $0.00 \leq x \leq 0.10$ , superconducting samples, where  $R = \text{Sm}$  and  $\text{La}$

$x$	$\alpha$ (m $\Omega$ .cm/K)	$T_0$ (K)	$T_c$ (K)	$T^*$ (K)	$\Delta T$ (K)	$\rho_0$ ( $\Omega$ .cm)	$\rho_n$ ( $\Omega$ .cm)
0.000	2.73	102.6	105.4	161.9	2.85	-0.071	0.736
<i>Sm Substitution</i>							
0.025	2.16	103.4	112.0	212.5	8.60	0.029	0.679
0.050	1.78	100.3	110.5	218.2	10.15	0.033	0.563
0.075	1.23	99.3	105.3	216.5	6.00	0.148	0.514
0.100	1.74	91.3	99.9	207.0	8.70	0.264	0.781
<i>La Substitution</i>							
0.025	2.25	105.8	116.7	208.3	10.90	0.096	0.706
0.050	1.04	102.1	109.5	157.2	7.40	0.050	0.360
0.075	3.16	99.3	106.5	175.1	7.20	0.086	1.016
0.100	2.45	97.0	105.2	184.9	7.80	0.170	0.893

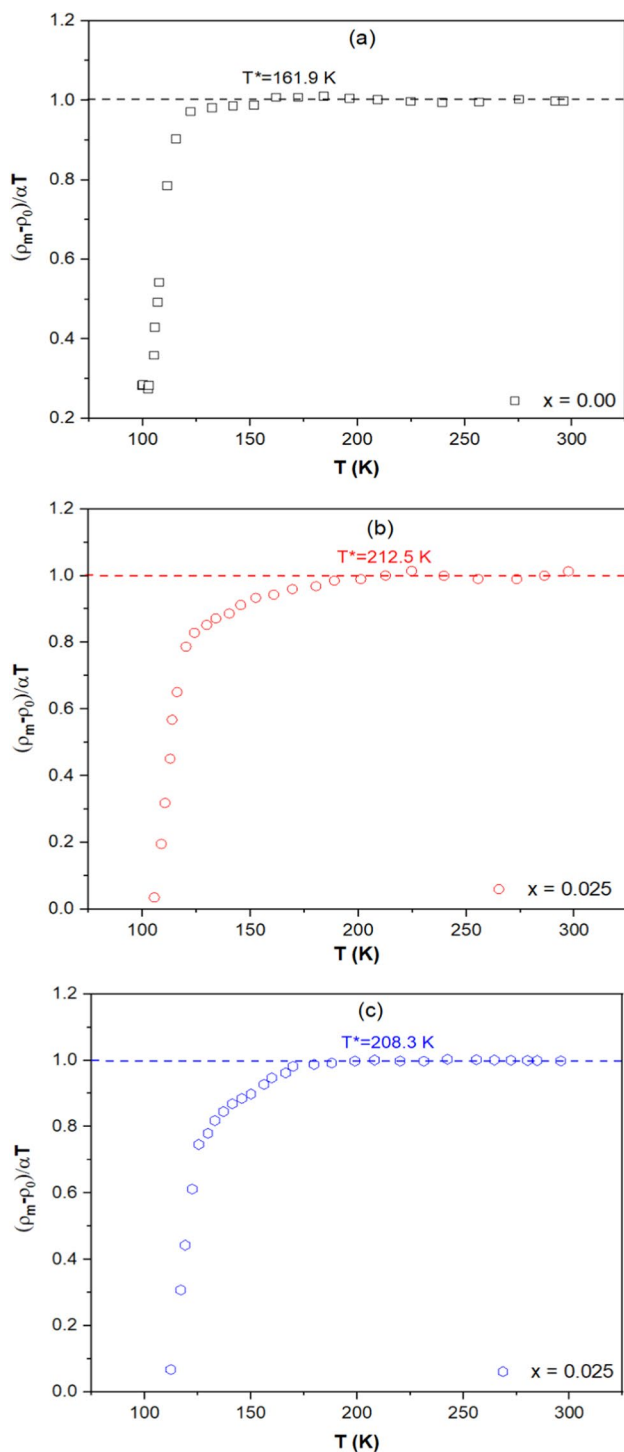


**Fig. 14** Graph of the  $T^*$  determination for  $\text{Tl}_{0.8}\text{Hg}_{0.2}\text{Ba}_2\text{Ca}_{2-x}\text{R}_x\text{Cu}_3\text{O}_{9-\delta-y}\text{F}_y$  using the criterion  $(\rho(T) - \rho_0)/\alpha T = 1$ , for (a)  $x = 0.00$ , (b) Sm substitution with  $x = 0.025$ , and (c) La substitution with  $x = 0.025$

increasing the substitution content within the material can increase inhomogeneity or phase separation [53]. Different superconducting qualities can be found in different locations

with varied local compositions or doping levels, resulting in a wider transition width.

### 3.5 Excess conductivity analysis

Fluctuation-induced conductivity analysis of conductivity data of  $\text{Tl}_{0.8}\text{Hg}_{0.2}\text{Ba}_2\text{Ca}_{2-x}\text{R}_x\text{Cu}_3\text{O}_{9-\delta-y}\text{F}_y$ , where  $R = \text{Sm}$  and  $\text{La}$ , were performed to explore the influence of substituted Sm and La-atoms on inherent superconducting characteristics. The small curvature found in electrical resistivity measurements for all samples above  $T_c$ , known as excess conductivity, was explained using thermodynamic fluctuations in the superconducting order parameter. The superconducting fluctuations are caused by two major mechanisms. The direct process, initially postulated by Aslamazov and Larkin (AL), is caused by the acceleration of superconducting pairs with finite lifetimes generated in thermal non-equilibrium [54]. The scattering of normal-state quasiparticles by superconducting pairs results in another indirect mechanism which is elucidated by Maki and Thompson (MT) [55].

The excess conductivity  $\Delta\sigma$  is defined by [56]:

$$\Delta\sigma = \sigma_m(T) - \sigma_n(T) = \frac{1}{\rho_m(T)} - \frac{1}{\rho_n(T)}, \quad (2)$$

where  $\rho_m(T)$  is the measured resistivity and  $\rho_n(T)$  is the normal-state resistivity.

In the mean-field region (MFR), where the variations are minor, the normalized excess conductivity  $\frac{\Delta\sigma}{\sigma_{room}}$  was estimated using AL:

$$\frac{\Delta\sigma}{\sigma_{room}} = C t^z, \quad (3)$$

where  $t = \frac{T - T_c}{T_c}$  is a reduced temperature, and  $z$  is a critical exponent. Its value differentiates between critical (cr), three-dimensional (3D), two-dimensional (2D), and short-wave (sw) fluctuation regions, and it is given by [57–59]:

$$z = \begin{cases} -0.3 & \text{For (cr) fluctuations,} \\ -0.5 & \text{For (3D) fluctuations,} \\ -1.0 & \text{For (2D) fluctuations,} \\ -3.0 & \text{For (sw) fluctuations.} \end{cases} \quad (4)$$

Figures 15 and 16a–e illustrate the normalized excess conductivity as a function of reduced temperature  $t$  for  $\text{Tl}_{0.8}\text{Hg}_{0.2}\text{Ba}_2\text{Ca}_{2-x}\text{R}_x\text{Cu}_3\text{O}_{9-\delta-y}\text{F}_y$ , where  $R = \text{Sm}$  and  $\text{La}$ , respectively, with  $0.00 \leq x \leq 0.10$ . Each figure clearly depicted four separate zones. The plots are linearly fitted to compare the experimental data to theoretical predictions. The values for the conductivity exponent  $z$  are obtained from the slopes and presented in Table 4. In the first region, the normalized excess conductivity falls sharply with  $z_{sw} \approx -3$  in the first zone. This drop is caused by a change in

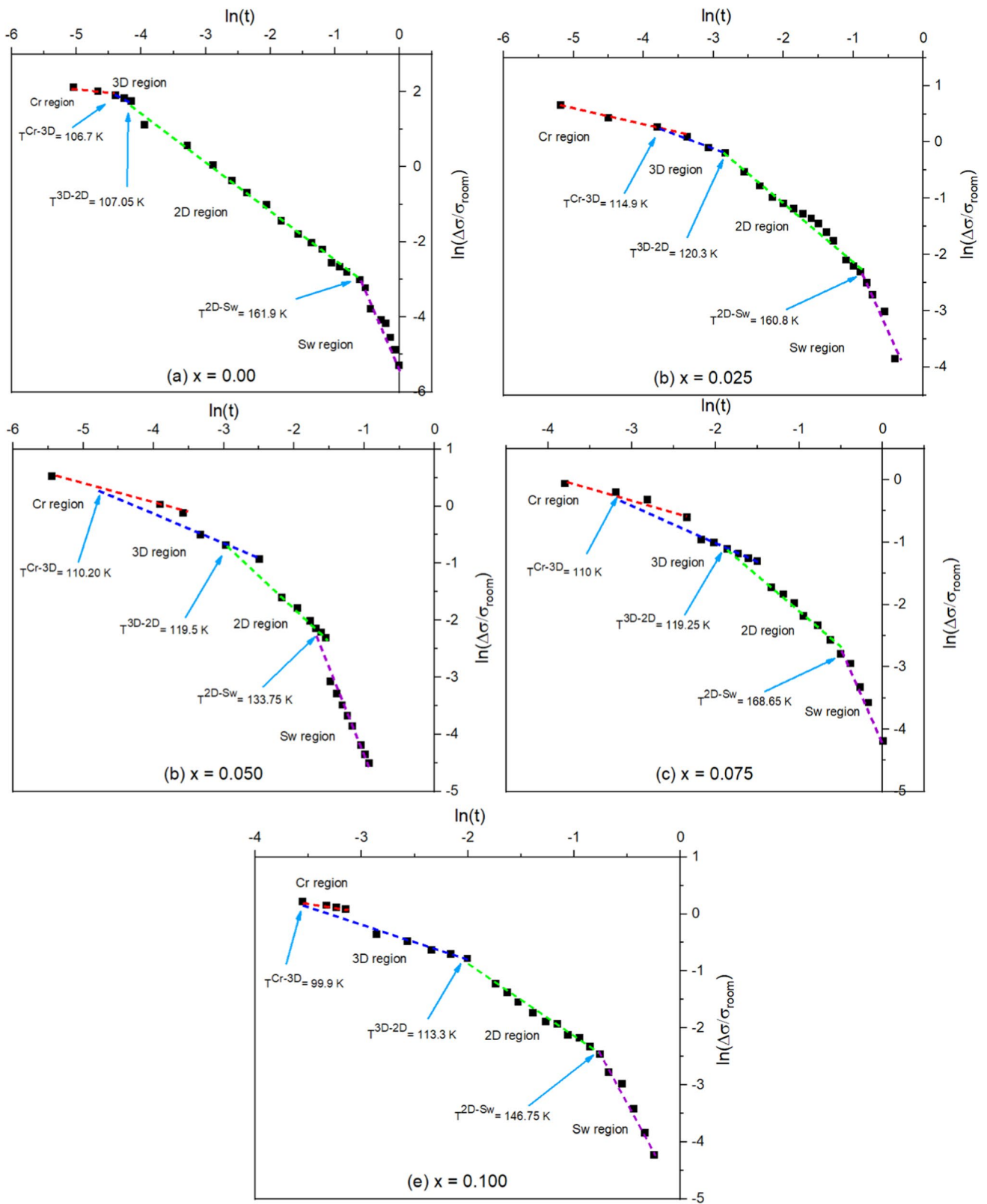


**Fig. 15** The variation of the normalized excess conductivity  $\Delta\sigma/\sigma_{\text{room}}$  with the reduced temperature  $t$  in the  $\ln$ - $\ln$  plot for  $\text{Ti}_{0.8}\text{Hg}_{0.2}\text{Ba}_2\text{Ca}_{2-x}\text{Sm}_x\text{Cu}_3\text{O}_{9-\delta-y}\text{F}_y$  with (a)  $x = 0.00$ , (b)  $x = 0.025$ , (c)  $x = 0.050$ , (d)  $x = 0.075$ , and (e)  $x = 0.100$



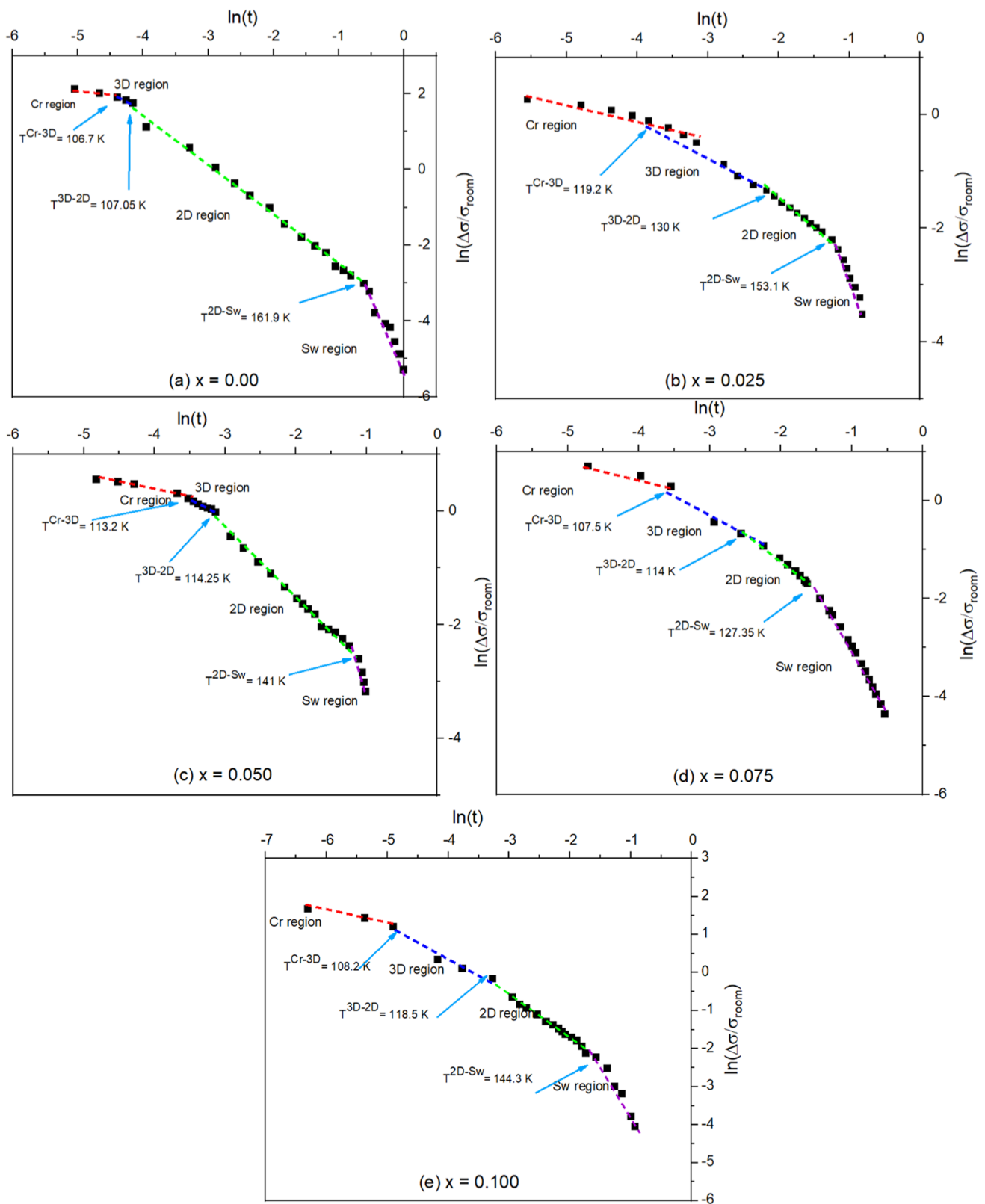


**Fig. 16** The variation of the normalized excess conductivity  $\Delta\sigma/\sigma_{\text{room}}$  with the reduced temperature  $t$  in the  $\ln$ - $\ln$  plot for  $\text{Tl}_{0.8}\text{Hg}_{0.2}\text{Ba}_2\text{Ca}_{2-x}\text{La}_x\text{Cu}_3\text{O}_{9-\delta-y}\text{F}_y$  with (a)  $x = 0.00$ , (b)  $x = 0.025$ , (c)  $x = 0.050$ , (d)  $x = 0.075$ , and (e)  $x = 0.100$ .

**Table 4** The variation of conductivity exponents with the substitution content for  $\text{Tl}_{0.8}\text{Hg}_{0.2}\text{Ba}_2\text{Ca}_{2-x}\text{R}_x\text{Cu}_3\text{O}_{9.8-y}\text{F}_y$ , where R=Sm and La for  $0.00 \leq x \leq 0.10$ 

$x$	$Z$ (sw)	$Z$ (3D)	$Z$ (2D)	$Z$ (cr)	$\xi_c(0)(\text{\AA})$	$d$ (Å)	$I \times 10^{-2}$	$v_f \times 10^4$ (m/s)	$E_f$ (eV)
0.00	-3.34	-0.49	-1.19	-0.31	4.25	57.02	0.5	3.22	0.030
Sm substitution									
0.025	-3.23	-0.53	-1.13	-0.30	4.00	23.60	2.8	3.23	0.031
0.050	-3.08	-0.51	-1.15	-0.33	4.50	33.33	1.8	3.58	0.037
0.075	-3.11	-0.54	-1.28	-0.35	5.11	35.90	2.0	3.87	0.044
0.100	-3.35	-0.51	-1.21	-0.34	5.91	48.00	1.5	4.25	0.053
La substitution									
0.025	-3.38	-0.56	-1.08	-0.30	4.16	30.39	1.8	3.50	0.035
0.050	-3.25	-0.53	-1.20	-0.30	5.75	57.85	1.0	4.54	0.060
0.075	-3.13	-0.55	-1.15	-0.33	6.50	61.00	1.1	4.97	0.072
0.100	-3.06	-0.52	-1.10	-0.31	8.25	63.33	1.7	6.25	0.115

normal resistivity, and therefore a change in oxygen content, which is linked to a change in the band structure and hence the position of the Fermi level [60]. By decreasing the temperature, at a temperature  $T^{2D-sw}$ , a cross-over between short-wave fluctuations and the mean-field region is observed. The mean-field region is characterized by two distinct sections. In the first part, at temperatures exceeding  $T^{3D-2D}$ , the range of conductivity exponent values is from -1.10 to -1.28, indicating the existence of 2D fluctuations. The conductivity exponent values vary from -0.49 to 0.56 at lower temperatures than  $T^{3D-2D}$ , showing the presence of 3D fluctuations. The cross-over temperatures  $T^{3D-2D}$  were computed from the intersection of the two linear parts as shown in Figs. 15 and 16. In both replacements,  $T^{3D-2D}$  has the largest value for  $x = 0.025$  and then shifts to lower values as  $x$  increases.  $T^{3D-2D}$  is a critical parameter sensitive to the electronic structure in the normal state and may be severely impacted by high Sm and La content [51].

In the (2D) region, the charge carriers move along the molecular planes within the material. Conversely, in the (3D) area, they move across the planes and are more susceptible to thermal variations. As a result, before the creation of Cooper pairs, charge carriers tended to move more freely in the entire sample. Finally, at  $T^{r-3D}$ , a transition between three-dimensional and critical fluctuation occurred. The conductivity exponent values at the critical zone range from -0.30 to -0.31. These values align with the expectations of the 3D-xy universality class, characterized by dynamics provided by the representative E-model [61].

Finally,  $C$  is the temperature-independent amplitude, which is given in 3D and 2D by [52, 62, 63]:

$$C_{3D} = \frac{e^2}{32\hbar\xi_c(0)\sigma_{room}}, \quad (5)$$

and

$$C_{2D} = \frac{e^2}{16\hbar d\sigma_{room}}, \quad (6)$$

where  $\xi_c(0)$  is the zero-temperature coherence length along the  $c$ -axis, and  $d$  is the effective layer thickness of the 2D system. The interlayer coupling ( $I$ ), Fermi velocity ( $v_f$ ), and Fermi energy ( $E_f$ ) of the carriers are estimated from the following relations [25]:

$$I = \left[ \frac{\xi_c(0)}{d} \right]^2, \quad (7)$$

$$v_f = \frac{3.5\pi\xi_c(0)k_B T_c}{2\hbar}, \quad (8)$$

and

$$E_f = \frac{1}{2}m^*v_f^2, \quad (9)$$

where  $k_B$  is Boltzmann's constant,  $m^*$  is the effective mass of carriers (For Hg-1223  $m^* = 10 m_0$ ), and  $m_0$  is the carrier-free mass. The values of  $\xi_c(0)$ ,  $d$ ,  $I$ ,  $v_f$ , and  $E_f$  are computed and given in Table 4. The zero-temperature coherence length along the  $c$ -axis clearly rises with substitution content, and the value of the unsubstituted sample is greater than that found by Han et al. [64] in the (Hg, Tl)-1223 phase (1.24–1.3 Å). These findings can be explained by the basic grain model. Because ceramic samples are made up of particles with holes, microcracks, and stacking defaults, their transport behavior is complicated. This signifies that the inter-grain connections connect the distinct particles. Passos et al. [65] obtained similar findings in (Hg, Re)-1223. Furthermore, as shown in Table 4, the values of  $d$  and  $\xi_c(0)$

decrease up to  $x=0.025$  and subsequently increase when Sm and La content increases further. This outcome is related to an increase in core density and connection interlinking between grains, as shown in SEM micrographs [56]. Furthermore, the rise in  $\xi_c(0)$  along the c-axis implies that the unsubstituted sample resides in the over-doped region. It converts to the optimum-doped region at  $x=0.025$  and subsequently shifts to the under-doped region as the substitution contents increase [25]. Compared to the pure sample, samples with a smaller coherence length along the c-axis and a greater effective layer thickness exhibited an enhancement in interplanar coupling. All of the  $I$  values for the produced samples are less than 1, indicating that there is a weak connection between  $\text{CuO}_2$  planes and that the cross-over between 3 and 2D areas occurs [66]. For all prepared samples, the computed Fermi-velocities are smaller than that of the free electron ( $v_f = 10^6$  m/s). The unsubstituted sample's

Fermi velocity ( $0.845 \times 10^5$ ) is smaller than that obtained from magneto-conductivity analysis in the (Hg, Tl)-1223 phase [67]. The rise in Fermi energy with increasing substitution content is most likely owing to a change in the effective mass of carriers, demonstrating that the band structure of (Tl, Hg)-1223 is severely impacted by rare-earth [66].

### 3.6 I–V results

$J_c$  measurements at a low temperature (77 K) are used to evaluate the capacity of the produced superconducting samples to hold current. Figure 17a, b depicts the  $E$ – $J$  curves of  $\text{Tl}_{0.8}\text{Hg}_{0.2}\text{Ba}_2\text{Ca}_{2-x}\text{R}_x\text{Cu}_3\text{O}_{9-\delta-y}\text{F}_y$  with  $x = 0.00, 0.025, 0.050, 0.075,$  and  $0.10$  for  $R = \text{Sm}$  and  $\text{La}$ , using a threshold of  $1 \mu\text{V}/\text{cm}$  [68]. The  $E$ – $J$  curves were created using the power-law relation provided by [69]:  $E = \beta J^n$ , where  $\beta$  and  $n$  are experimental constants. Additionally, Fig. 18a, b illustrates

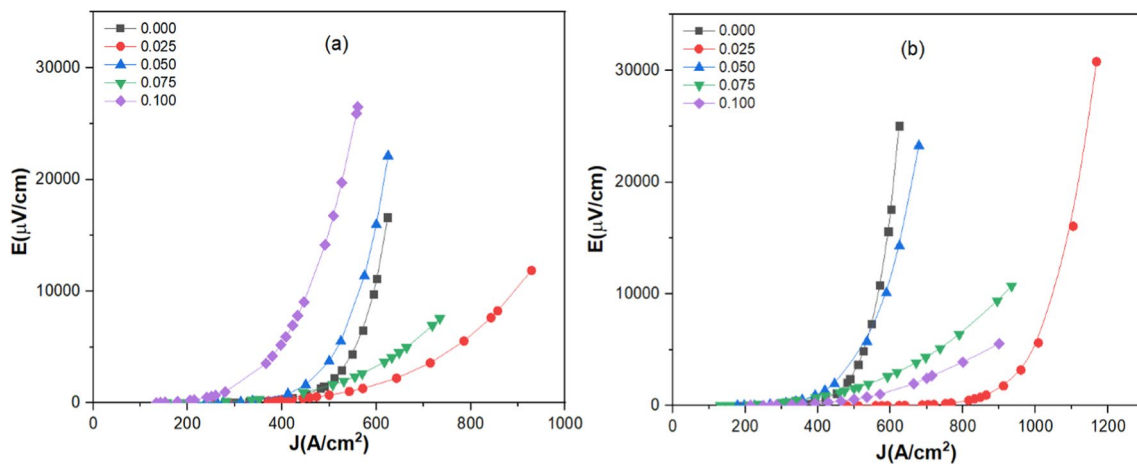


**Fig. 17**  $E$ – $J$  curve for  $\text{Tl}_{0.8}\text{Hg}_{0.2}\text{Ba}_2\text{Ca}_{2-x}\text{R}_x\text{Cu}_3\text{O}_{9-\delta-y}\text{F}_y$ ,  $0.00 \leq x \leq 0.10$ , superconducting samples: (a)  $R = \text{Sm}$  and (b)  $R = \text{La}$

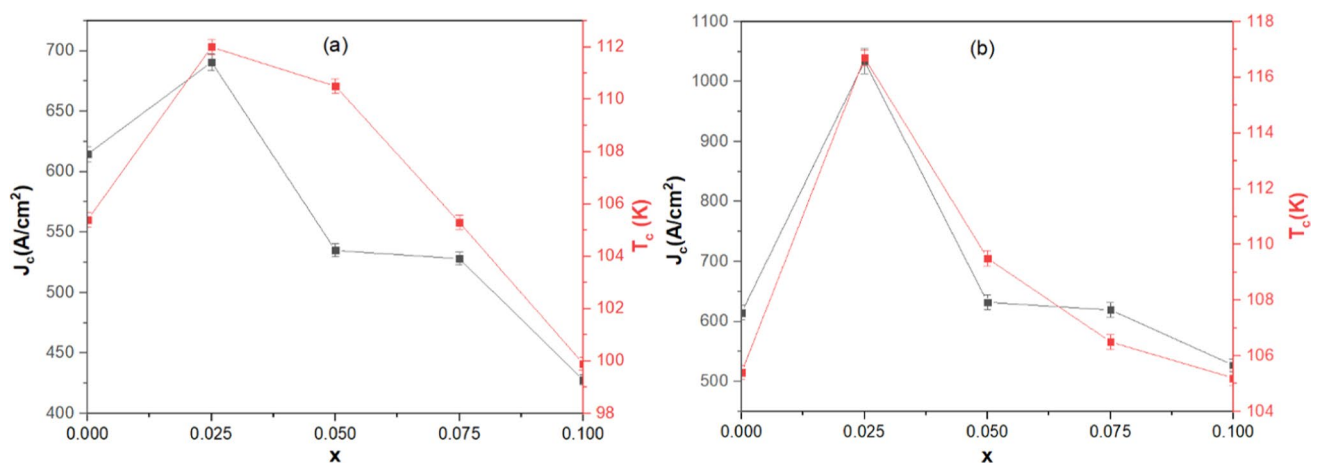


**Fig. 18** Variations of  $T_c$  and  $J_c$  as a function of  $x$  for  $\text{Tl}_{0.8-x}\text{Hg}_{0.2}\text{Ba}_2\text{Ca}_{2-x}\text{R}_x\text{Cu}_3\text{O}_{9-\delta-y}\text{F}_y$  phase for (a)  $R = \text{Sm}$  and (b)  $R = \text{La}$

the link between  $T_c$  and  $J_c$  of the prepared samples as a function of Sm and La content. Clearly,  $J_c$  followed the same trend as  $T_c$  with  $x$ . According to observations from Figs. 17 and 18, it is evident that  $J_c$  exhibits a gradual increase in both replacements up to  $x = 0.025$ .  $J_c$  increases from approximately 614 A/cm<sup>2</sup> for the pure sample to 691 A/cm<sup>2</sup> at a rate of 12.5% and 1034 A/cm<sup>2</sup> at a rate of 68.4% of Sm and La, respectively. This enhancement may be attributable to Sm and La replacements acting as pinning centers to fix vortices and boost inter-grain connection and inter-granular flux pinning [71, 72]. It is worth mentioning that La has a more pronounced effect than Sm in enhancing the flux pinning and critical current density of the prepared samples. This is likely attributed to lattice defects generated by the partial substitution of La<sup>3+</sup> with Ca<sup>2+</sup>, which proves to be more effective than the substitution of Sm<sup>3+</sup> with Ca<sup>2+</sup>, which can increase flux pinning and grain coupling [17]. On contrary, when Sm and La contents increase ( $x > 0.025$ ),  $J_c$  decreases and reaches 427 A/cm<sup>2</sup> and 527 A/cm<sup>2</sup> for  $x = 0.10$ . This can be attributed to various factors, such as a rise in impurity content, the presence of voids between grain as well as grain alignment disorder and reduction in inter-grain connection [49, 72].

## 4 Conclusion

In the present study, Tl<sub>0.8</sub>Hg<sub>0.2</sub>Ba<sub>2</sub>Ca<sub>2-x</sub>R<sub>x</sub>Cu<sub>3</sub>O<sub>9-δ-y</sub>F<sub>y</sub>, where R = Sm and La samples ( $x = 0.00, 0.025, 0.050, 0.075$ , and  $0.100$ ) were effectively prepared by solid-state reaction technique. The XRD demonstrated that both types of substitutions have no effect on the tetragonal crystal structure of the (Tl, Hg)-1223 superconducting phase. Furthermore, the volume fraction was increased from 75.95% to 91.10%, and 92.37% when  $x$  increased up to 0.025 for SmF<sub>3</sub> and LaF<sub>3</sub> substitutions, respectively. SEM images demonstrated that the substitution of Sm and La up to 0.025 improved the morphology and structure of the sample. The Sm, La, and F atoms doped into the (Tl, Hg)-1223 phase replaced the Ca and O atoms as desired, according to EDX results. Furthermore, XPS studies revealed that the superconductivity of (Tl, Hg)-1223 was controlled by an electron transfer process. An improvement in  $T_c$  and  $J_c$  by Sm and La substitutions up to  $x = 0.025$  was confirmed by the resistivity measurements and  $I-V$  characteristics, respectively. The increase in  $T_c$  was ascribed to the improvement of the grain's connectivity and the transition from over-doped to optimum-doped samples. The excess conductivity investigation indicated the presence of four fluctuation zones close and above  $T_c$  (cr, 3D, 2D, and sw). The values of  $\xi_c(0)$ ,  $d$ ,  $I$ ,  $v_f$ , and  $E_f$  were computed using the AL model. The calculated zero-temperature coherence length along the  $c$ -axis for the unsubstituted sample was greater than those obtained for single crystal and

highly aligned grains samples, indicating the complex transport behavior of ceramic materials. Finally, all the findings showed that, under our preparation conditions, the replacement of Sm and La with  $x = 0.025$  was thought to be the optimal quantity to enhance the superconducting properties for the (Tl, Hg)-1223 phase. In comparison to the substitution with SmF<sub>3</sub>, the substitution with LaF<sub>3</sub> proved to be more effective in increasing volume fraction,  $T_c$ , and  $J_c$ . This is due to the unique ionic size and electronic structure of La<sup>3+</sup>, which have a beneficial effect on the formation and stability of Cooper pairs. These improvements are critical in the development of the material's superconducting properties.

**Acknowledgements** This work was done in the Faculty of Science, Beirut Arab University, at the Specialized Materials Science Laboratory, Physics Department, in collaboration with the Faculty of Science at Alexandria University in Alexandria, Egypt.

**Author contributions** Conceptualization: [RA, RFKK]; methodology: [RFK, KH]; formal analysis and investigation: [RFK, MA, KH]; writing—original draft preparation: [RFK]; writing—review and editing: [RA, KH, MA]; Validation: [RFK, MA, KH]; Supervision: [RA, MA, KH].

**Funding** The authors did not receive any funding from any organization for this study.

**Data availability** This article includes all data produced or analyzed during this study.

## Declarations

**Conflict of interest** The authors have no competing interests that are relevant to the content of this work to disclose.

## References

1. E.K. Al-Shakarchi, A.I. Al-Janabi, J. Supercond. Novel Magn. **33**, 379 (2020)
2. A. Cigáň, G. Plesch, M. Škrátek, M. Kopčok, J. Maňka, P. Jurdák, and A. Koňakovský, Open Physics **9**, (2011).
3. R. Giri, H.K. Singh, R.S. Tiwari, O.N. Srivastava, Bull. Mater. Sci. **24**, 523 (2001)
4. T. Oku, S. Nakajima, Solid State Commun. **124**, 305 (2002)
5. I. Metskhvarishvili, T. Lobzhanidze, G. Dgebuadze, B. Bendeliani, M. Metskhvarishvili, M. S. Rusia, V. Gabunia, and K. Komakhidze, (2020).
6. S. Lee, T. Akao, N. Kiryakov, H. Suematsu, H. Yamauchi, Physica C **338**, 60 (2000)
7. M. Giebułtowski, R. Zalecki, M. Rajska, W. Tokarz, J. M. Michalik, M. Kowalik, and W. M. Woch, Ceramics International **47**, 18998 (2021).
8. K. M. Wadi, R. K. Chillab, A. N. Abdulateef, K. A. Jasim, A. H. Shaban, M. A. Hassan, and S. S. Jahil, in *Journal of Physics: Conference Series* (IOP Publishing, 2021), p. 032064.
9. M. Arif, M. Rahim, N.A. Khan, Ceram. Int. **46**, 3218 (2020)
10. N.A. Khan, A. Javaid, A.A. Khurram, N. Haider, Physica C **425**, 90 (2005)
11. E. Erbilien, Ş Çavdar, H. Koralay, A. Günen, Physica B **413**, 36 (2013)

12. Y. Boudjadja, A. Amira, A. Saoudeh, N. Mahamdoua, A. Varilci, C. Terzioğlu, S.P. Altintas, *Bol Soc Esp Ceram Vidr* **55**, 202 (2016)
13. R. Awad, I. H. Ibrahim, E. M. E. Mansour, M. Roumie, and A. Zein, in *Journal of Physics: Conference Series* (IOP Publishing, 2008), p. 012323.
14. M. Roumié, R. Awad, I.H. Ibrahim, A. Zein, K. Zahraman, B. Nsouli, *Nucl. Instrum. Methods Phys. Res., Sect. B* **266**, 133 (2008)
15. I.P.A. Bakar, K. Muhammad-Aizat, J. Nur-Akasyah, M.S. Mohd-Syahmi, M. Suib, N. Raihan, W.S. Chiu, R. Abd-Shukor, *Appl. Phys. A* **125**, 1 (2019)
16. R. Awad, A. Al-Zein, M. Roumie, I.H. Ibrahim, *J. Mater. Sci. Technol.* **29**, 1079 (2013)
17. A.I. Abou-Aly, R. Awad, I.H. Ibrahim, W. Abdeen, *J. Alloy. Compl.* **481**, 462 (2009)
18. V. G. Prabhitha, A. Biju, R. G. Abhilash Kumar, P. M. Sarun, R. P. Aloysius, and U. Syamaprasad, *Physica C: Superconductivity* **433**, 28 (2005).
19. R. Awad, A.I. Abou-Aly, I.H. Ibrahim, W. Abdeen, *Solid State Commun.* **146**, 92 (2008)
20. A.I. Abou-Aly, R. Awad, M. Kamal, M. Anas, *J. Low Temp. Phys.* **163**, 184 (2011)
21. A. Sedky, A. Salah, *J. Electron. Mater.* **51**, 3042 (2022)
22. N.M. Hamdan, Kh.A. Ziq, A.S. Al-Harthi, *Physica C* **314**, 125 (1999)
23. M. Anas, *Chem. Phys. Lett.* **742**, 137033 (2020)
24. H. AbuHlaiwa, H. Basma, M. Rekaby, M. Roumie, R. Awad, *J. Low Temp. Phys.* **198**, 26 (2020)
25. A. Kamar, A. Srour, M. Roumié, W. Malaeb, R. Awad, A. Khalaf, *Appl. Phys. A* **127**, 579 (2021)
26. A. Saoudeh, A. Saoudeh, Y. Boudjadja, H. Bouchehou, H. Allag, S.P. Altintas, *Cryogenics* **117**, 103326 (2021)
27. A.I. Abou-Aly, N.H. Mohammed, M. Roumié, A. El Khatib, R. Awad, S.A. Nour El Dein, *J. Supercond. Nov. Magn.* **22**, 495 (2009)
28. A. V. Narlikar, *High Temperature Superconductivity 1: Materials* (Springer Science & Business Media, 2004).
29. M.H. El Makdah, N. El Ghouch, M.H. El-Dakdouki, R. Awad, M. Matar, *Appl. Phys. A* **129**, 265 (2023)
30. R.A. Abbasi, N.A. Khan, Z. Malik, H.S. Raza, *J. Mater. Sci. Mater. Electron.* **32**, 9253 (2021)
31. M.H. El Makdah, N. El Ghouch, M.H. El-Dakdouki, R. Awad, M. Matar, *Ceram. Int.* **49**, 22400 (2023)
32. C.F. Holder, R.E. Schaak, *ACS Nano* **13**, 7359 (2019)
33. R. Cao, W. Wang, Y. Ren, Z. Hu, X. Zhou, Y. Xu, Z. Luo, A. Liang, *J. Lumin.* **235**, 118054 (2021)
34. E. G. Bae, J. Jeong, S. cheol Han, J. S. Kwak, and M. Pyo, *Meet. Abstr. MA2014-04*, 390 (2014).
35. R.F. Khattar, K. Habanjar, R. Awad, M. Anas, *J. Low Temp. Phys.* **211**, 166 (2023)
36. A.I.A. Aly, R. Awad, I.H. Ibrahim, M. Kamal, M. Anas, *J. Mater. Sci. Technol.* **28**, 169 (2012)
37. A. Khalid, P. Ahmad, A.I. Alharthi, S. Muhammad, M.U. Khandaker, M.R.I. Faruque, A. Khan, I.U. Din, M.A. Alotaibi, K. Alzimami, A.A. Alfuraih, D.A. Bradley, *Materials* **14**, 3223 (2021)
38. P. Kulkarni, S. Mahamuni, M. Chandrachood, I.S. Mulla, A.P.B. Sinha, A.S. Nigavekar, S.K. Kulkarni, *J. Appl. Phys.* **67**, 3438 (1990)
39. S. Marik, A. J. Dos santos-Garcia, C. Labrugere, E. Morán, O. Toulemonde, and M. A. Alario-Franco, *MRS Proc.* **1655**, mrsf13 (2014).
40. J. Jiang, X. Liu, J. Han, K. Hu, J. Chen, *Processes* **9**, 680 (2021)
41. C.-L. Hsiao, X. Qi, *Acta Mater.* **102**, 88 (2016)
42. L. Wang, J. Zhang, Q. Zhang, N. Xu, J. Song, *J. Magn. Magn. Mater.* **377**, 362 (2015)
43. V. Mariyappan, K. Murugan, S.-M. Chen, and B. Gopal, *Journal of the Electrochemical Society* **167**, (2020).
44. Z. Huang, J. Liu, L. Huang, L. Tian, S. Wang, G. Zhang, J. Li, F. Liang, H. Zhang, Q. Jia, S. Zhang, *NPG Asia Mater* **12**, 11 (2020)
45. H. Kumar and H. a P, *Tribology Transactions* **65**, 1 (2021).
46. Y. Mizuguchi, E. Paris, T. Wakita, G. Jinno, A. Puri, K. Terashima, B. Joseph, O. Miura, T. Yokoya, N.L. Saini, *Phys. Rev. B* **95**, 064515 (2017)
47. A. Esmaeili, H. Sedghi, M.M. Golzan, M. Amniat-Talab, *J. Supercond. Nov. Magn.* **24**, 2237 (2011)
48. M. Anas, G.A. El-Shorbagy, A.I. Abou-Aly, A. Khalaf, *J. Low Temp. Phys.* **206**, 210 (2022)
49. A. Nasser, A. Srour, N. El Ghouch, W. Malaeb, R. Al-Oweini, R. Awad, *Appl. Phys. A* **126**, 951 (2020)
50. M. Anas, G.A. El-Shorbagy, *J. Low Temp. Phys.* **194**, 183 (2019)
51. A. Abou Aly, I. Ibrahim, R. Awad, A. El-Harizy, and A. Khalaf, *Journal of Superconductivity & Novel Magnetism* **23**, (2010).
52. A. Aftabi, M. Mozaffari, *Sci. Rep.* **11**, 4341 (2021)
53. M. Leroux, V. Mishra, C. Opagiste, P. Rodière, A. Kayani, W.-K. Kwok, U. Welp, *Phys. Rev. B* **102**, 094519 (2020)
54. L.G. Aslamazov, A.I. Larkin, *Phys. Lett. A* **26**, 238 (1968)
55. K. Maki, R.S. Thompson, *Phys. Rev. B* **39**, 2767 (1989)
56. K. Habanjar, F.E.H. Hassan, R. Awad, *Mater. Res. Express* **6**, 096001 (2019)
57. S.A. Saleh, S.A. Ahmed, E.M.M. Elsheikh, *J. Supercond. Novel Magn.* **21**, 187 (2008)
58. S.H. Han, J. Axnäs, B.R. Zhao, Ö. Rapp, *Physica C* **408**, 679 (2004)
59. C.J. Lobb, *Phys. Rev. B* **36**, 3930 (1987)
60. A.K. Ghosh, A.N. Basu, *Phys. Rev. B* **59**, 11193 (1999)
61. P.C. Hohenberg, B.I. Halperin, *Rev. Mod. Phys.* **49**, 435 (1977)
62. A.K. Pradhan, S.B. Roy, P. Chaddah, C. Chen, B.M. Wanklyn, *Phys. Rev. B* **50**, 7180 (1994)
63. F. Sharifi, A.V. Herzog, R.C. Dynes, *Phys. Rev. Lett.* **71**, 428 (1993)
64. S.H. Han, I. Bryntse, J. Axnäs, B.R. Zhao, Ö. Rapp, *Physica C* **388**, 349 (2003)
65. C.A.C. Passos, M.T.D. Orlando, J.L. Passamai Jr., E.V.L. De Mello, H.P.S. Correa, L.G. Martinez, *Phys. Rev. B* **74**, 094514 (2006)
66. A.I. Abou-Aly, R. Awad, I.H. Ibrahim, W. Abdeen, *Solid State Commun.* **149**, 281 (2009)
67. J. Axnäs, I. Bryntse, I. Safonova, Ö. Rapp, *Physica B* **284**, 1009 (2000)
68. E. Seiler, F. Gömöry, J. Mišík, D. Richter, *Physica C* **551**, 66 (2018)
69. F. Vallès, A. Palau, V. Rouco, B. Mundet, X. Obradors, T. Puig, *Sci. Rep.* **8**, 5924 (2018)
70. S.F. Oboudi, *J. Supercond. Nov. Magn.* **30**, 1473 (2017)
71. N. Ghazanfari, A. Kılıç, A. Gencer, H. Özkan, *Solid State Commun.* **144**, 210 (2007)
72. E.S. Nurbaisyatul, H. Azhan, N. Ibrahim, S.F. Saipuddin, *Cryogenics* **119**, 103353 (2021)

**Publisher's Note** Springer Nature remains neutral with regard to jurisdictional claims in published maps and institutional affiliations.

Springer Nature or its licensor (e.g. a society or other partner) holds exclusive rights to this article under a publishing agreement with the author(s) or other rightsholder(s); author self-archiving of the accepted manuscript version of this article is solely governed by the terms of such publishing agreement and applicable law.